

High Reynolds number Taylor-Couette turbulence

Siegfried Grossmann¹, Detlef Lohse^{2,3},
and Chao Sun^{2,4}

¹Fachbereich Physik, University of Marburg, Renthof 6, D-35032 Marburg, Germany.

²Physics of Fluids Group, Faculty of Science and Technology, J.M. Burgers Center for Fluid Dynamics, and MESA+ Institute, University of Twente, The Netherlands. email addresses: d.lohse@utwente.nl; c.sun@utwente.nl.

³Max Planck Institute for Dynamics and Self-Organization, 37077 Göttingen, Germany

⁴Center for Combustion Energy and Department of Thermal Engineering, Tsinghua University, 100084 Beijing, China

xxxxxx 0000. 00:1–30
Copyright © 0000 by Annual Reviews.
All rights reserved

Keywords

Rotating flow, fully developed turbulence, laminar & turbulent boundary layers, transport properties, quasi-Keplerian flows

Abstract

Taylor-Couette flow – the flow between two coaxial co- or counter-rotating cylinders – is one of the paradigmatic systems in physics of fluids. The (dimensionless) control parameters are the Reynolds numbers of the inner and outer cylinder, the ratio of the cylinder radii, and the aspect ratio. The response of the system is the torque required to retain constant angular velocities, which can be connected to the angular velocity transport through the gap. While the low Reynolds number regime has been very well explored in the '80s and '90s of the last century, in the fully turbulent regime major research activity only developed in the last decade. In this paper we review this recent progress in our understanding of fully developed Taylor-Couette turbulence, from the experimental, numerical, and theoretical point of view. We will focus on the parameter dependence of the global torque and on the local flow organisation, including velocity profiles and boundary layers. Next, we will discuss transitions between different (turbulent) flow states. We will also elaborate on the relevance of this system for astrophysical disks (Keplerian flows). The review ends with a list of challenges for future research on turbulent Taylor-Couette flow.

The published version in ARFM: Annu. Rev. Fluid Mech. 48:53-80 (2016).

1. Introduction

Taylor-Couette (TC) flow, the flow between two coaxial, independently rotating cylinders (as sketched in figure 1), is one of the paradigmatic systems of physics of fluids. It is, next to Rayleigh-Bénard (RB) flow (the flow in a box heated from below and cooled from above), the ‘drosophila’ of the field, and various new concepts in fluid dynamics have been tested with these systems, be it instabilities (e.g. Taylor 1923; Coles 1965; Chandrasekhar 1981; Drazin & Reid 1981; DiPrima & Swinney 1981; Busse 1967; Coughlin & Marcus 1996; Marques & Lopez 1997; Hristova et al. 2002; Meseguer 2002; Donnelly 1991; Gebhardt & Grossmann 1993; Tuckerman 2014; Maretzke, Hof & Avila 2014), nonlinear dynamics and spatio-temporal chaos (e.g. Lorenz 1963; Ahlers 1974; Pfister & Rehberg 1981; Smith & Townsend 1982; Behringer 1985; Mullin, Cliffe & Pfister 1987; Strogatz 1994), pattern formation (e.g. Cross & Hohenberg 1993; Andereck, Liu & Swinney 1986; Koschmieder 1993; Büchel et al. 1996; Bodenschatz, Pesch & Ahlers 2000), or turbulence (e.g. Siggia 1994; Kadanoff 2001; Lathrop, Fineberg & Swinney 1992b; Ahlers, Grossmann & Lohse 2009; Lohse & Xia 2010). The reasons why these systems are so popular are from our point of view: (i) They are mathematically well-defined by the Navier-Stokes equations with their respective boundary conditions. (ii) For these closed system exact global balance relations between the respective driving and the dissipation can be derived. (iii) They are experimentally accessible with high precision, thanks to the simple geometries and high symmetries. (iv) The boundaries and resulting boundary layers play a prominent role and thus they are ideal systems to study the interaction between boundary layers and bulk. (v) There is a close analogy of RB and TC flow with pipe flow (as e.g. elaborated in Eckhardt, Grossmann & Lohse 2000, 2007a), which from a technological point of view may be the most important turbulent flow. So insight into the interaction between boundary layers and bulk in TC and RB turbulence will clearly also shed more light on the pipe flow problem (see e.g. Zagarola & Smits 1998; Marusic et al. 2010; Hultmark et al. 2012).

In the 1980s much research was done on TC flow for small Reynolds numbers, at onset of the instabilities and slightly above, in parallel to related work for RB flow. In this regime – in spite of the low Reynolds numbers up to only 1000 or 2000 – the flow structure is extremely rich, as reflected in the phase diagram of Andereck, Liu & Swinney (1986), which we reproduce in figure 2. In a nutshell, TC flow is linearly stable for outer cylinder rotation and fixed or only slowly rotating inner cylinder. The onset of instabilities at increasing Reynolds number of the inner cylinder is caused by the driving centrifugal force and can be estimated by force balance arguments as done by Taylor (1923); Esser & Grossmann (1996), who generalized Rayleigh’s famous stability criterion (Lord Rayleigh 1917). In the unstable regime one can observe Taylor rolls, modulated waves, spirals, and many other rich spatial and temporal flow features. For more details on this regime we refer to the book by Chossat & Iooss (1994), to the recent review by Fardin, Perge & Taberlet (2014), and to the review given in the thesis by Borrero-Echeverry (2014).

While in the 1990s for RB flow the degree of turbulence was continuously increased both experimentally with various setups and numerically with several codes (see e.g. the reviews by Siggia 1994; Ahlers, Grossmann & Lohse 2009; Lohse & Xia 2010), for TC flow there was much less activity, the most visible exception being the Austin-Maryland experiment by Lathrop, Fineberg & Swinney (1992b,a); Lewis & Swinney (1999), who experimentally explored fully developed TC turbulence for pure inner cylinder rotation. For *independently* rotating cylinders and at the same time strongly driven turbulence, up to a few years ago the experiments by Wendt (1933) remained the most prominent ones.

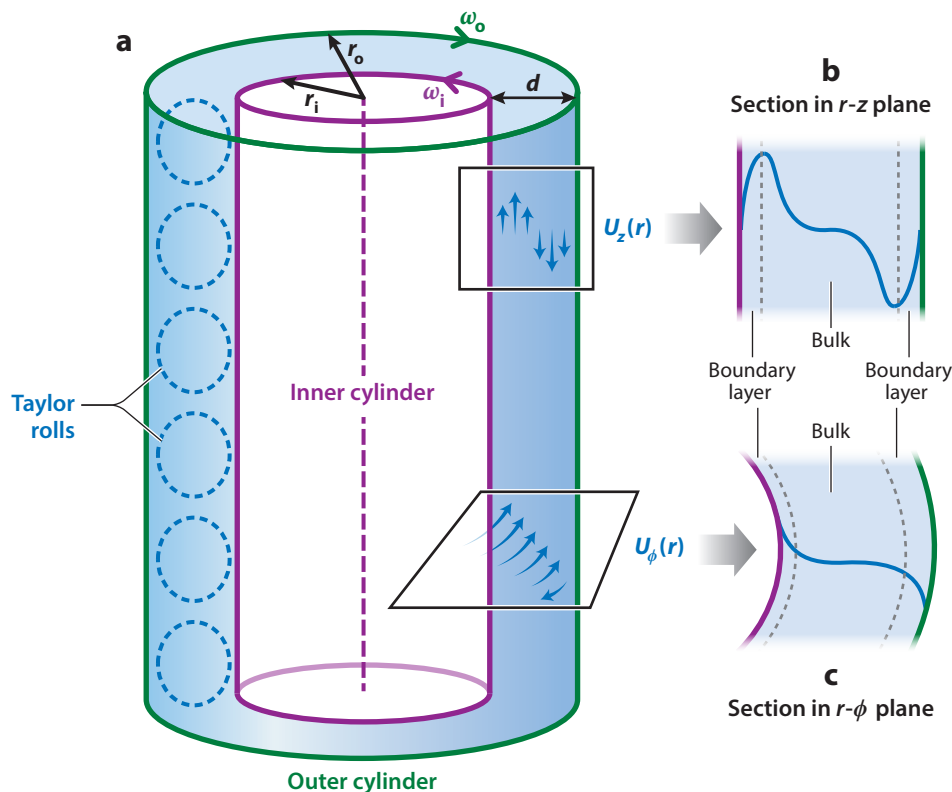


Figure 1

(a) Sketch for Taylor-Couette flow and the notation used in the present work. The inner and outer cylinder radii are r_i and r_o , respectively, their respective angular velocities are ω_i and ω_o . The gap width is $d = r_o - r_i$. Radial distances from the origin are called r . The mean azimuthal velocity field is $U_\phi(r) = r\Omega(r)$, where $\Omega(r)$ is the angular velocity. The mean axial velocity field is $U_z(r)$, which besides on r will also depend on the axial position z . The dashed rolls indicate the Taylor roll remnants with axial and radial velocity components, which are considered to be the largest eddies of the turbulent TC flow. A sketch of (b) the axial velocity and (c) the azimuthal velocity profile in the boundary layers (BL) and the bulk.

This situation has only changed in the last decade, when researchers started to explore the full phase space of TC, i.e. also for independently rotating cylinders and in the strongly turbulent regime, well beyond the onset of chaos. Many new experimental setups have been built to examine various aspects of strongly turbulent TC flow with co- and counter-rotating cylinders (Ji et al. 2006; Ravelet, Delfos & Westerweel 2010; Borrero-Echeverry, Schatz & Tagg 2010; van Gils et al. 2011a,b, 2012; van Hout & Katz 2011; Paoletti & Lathrop 2011; Schartman et al. 2012; Huisman et al. 2012; Merbold, Brauckmann & Egbers 2013; Huisman, Lohse & Sun 2013; Huisman et al. 2013, 2014) and correspondingly numerical simulations have been pushed to very high Reynolds numbers (He, Tanahashi & Miyauchi 2007; Bilson & Bremhorst 2007; Dong 2007, 2008; Pirro & Quadrio 2008; Brauckmann & Eckhardt 2013a,b;

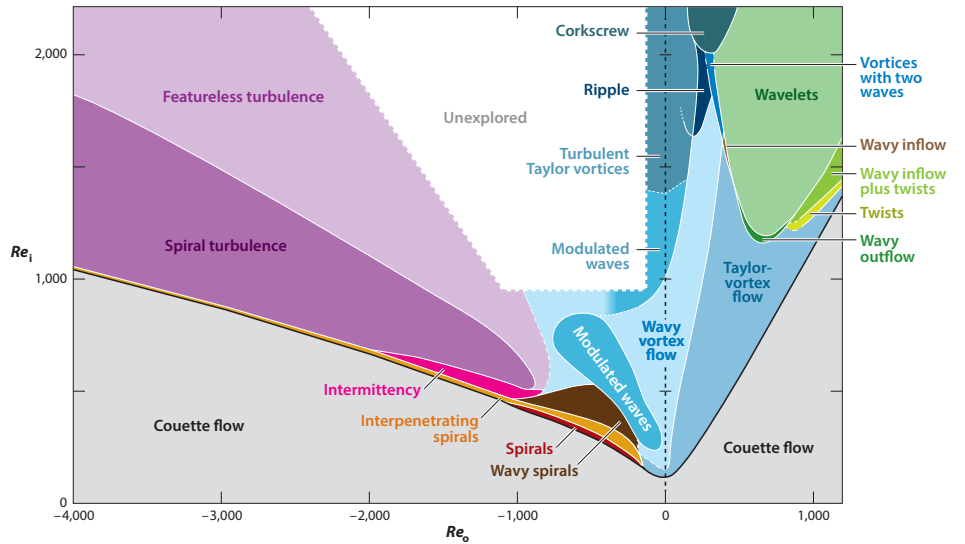


Figure 2

Observed rich flow structures in the (Re_o, Re_i) phase diagram for TC flow at $\eta = 0.833$. Figure taken from Andereck, Liu & Swinney (1986), with permission from the authors.

Ostilla-Mónico et al. 2013, 2014a,b,c; Chouippe et al. 2014). Figure 3 shows the currently explored parameter space in different representations. These phase diagrams clearly indicate that the field of high Reynolds number TC flow has been progressing rapidly and it is the aim of this article to review this progress.

The review is organized as follows: In section 2 we introduce the control parameter space of TC flow and its global response. A general overview of the flow organization in different regimes of the parameter spaces is given in section 3, together with the central idea of how to calculate the global response – namely a partitioning of the flow into a boundary layer and a bulk part entirely analogously to what has been done in RB flow (Grossmann & Lohse 2000, 2001, 2002, 2004). In section 4 we report on the global response of the system. The detailed local flow organization – profiles and rolls – is described in section 5, resulting in an explanation of when and why the system displays optimal transport properties. In that section we will also report on the occurrence of multiple turbulent states in TC flow. While these first sections focus on the Rayleigh unstable regime, we touch upon the Rayleigh stable regime in section 6, due to its relevance for astrophysical models. The review ends with a summary and an outlook on open issues (section 7).

2. Control parameters and global response of Taylor-Couette flow

The geometric parameters describing the TC system are the inner and the outer cylinder radii r_i and r_o , respectively, the corresponding gap width $d = r_o - r_i$, and the height L of the sample, see figure 1. In dimensionless form these parameters are expressed via the radius ratio $\eta = r_i/r_o$ and the aspect ratio $\Gamma = L/d$. The driving of the system is

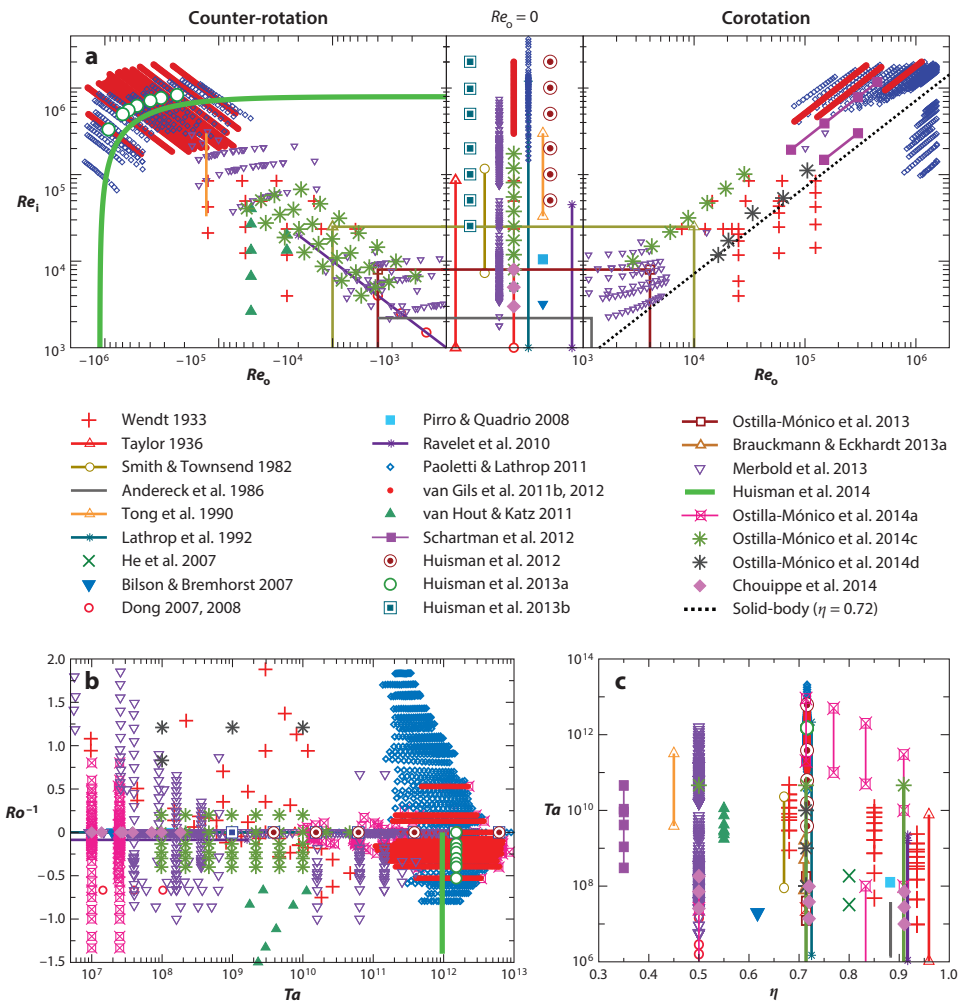


Figure 3

(a) Explored (Re_o , Re_i) parameter space of TC flow with independently rotating inner and outer cylinders. Both experimental data (Wendt 1933; Taylor 1936; Smith & Townsend 1982; Andereck, Liu & Swinney 1986; Tong et al. 1990; Lathrop, Fineberg & Swinney 1992a; Ravelet, Delfos & Westerweel 2010; van Gils et al. 2011b, 2012; van Hout & Katz 2011; Paoletti & Lathrop 2011; Schartman et al. 2012; Huisman et al. 2012; Merbold, Brauckmann & Egbers 2013; Huisman, Lohse & Sun 2013; Huisman et al. 2013, 2014) and numerical data (He, Tanahashi & Miyauchi 2007; Bilson & Bremhorst 2007; Dong 2007, 2008; Pirro & Quadrio 2008; Brauckmann & Eckhardt 2013a; Ostilla-Mónico et al. 2013, 2014a,c; Chouippe et al. 2014) are shown. The solid-body rotation line for a radius ratio $\eta = 0.71$ is added. Solid lines between markers represent a large density of experiments. In (b) the same data are shown in the (Ta , Ro^{-1}) parameter space and in (c) the explored (η , Ta) parameter space is shown. These phase diagrams clearly indicate that the field of high Reynolds number TC flow has been progressing rapidly.

through rotation of the inner and outer cylinder. In dimensional form this is quantified by the angular velocities ω_i and ω_o , and in dimensionless form by the respective Reynolds numbers Re_i and Re_o , namely

$$Re_{i,o} = \frac{r_{i,o}\omega_{i,o}d}{\nu}, \quad (1)$$

where ν is the kinematic viscosity of the fluid in between the cylinders. The convention is that Re_i is always positive, whereas $Re_o > 0$ stands for a co-rotating and $Re_o < 0$ for a counter-rotating outer cylinder.

Instead of using Re_i and Re_o , alternatively the driving of TC flow can be characterized by the Taylor number

$$Ta = \frac{(1 + \eta)^4}{64\eta^2} \frac{(r_o - r_i)^2 (r_i + r_o)^2 (\omega_i - \omega_o)^2}{\nu^2}, \quad (2)$$

which can be seen as the non-dimensional differential rotation of the system, and the (negative) rotation ratio $a = -\omega_o/\omega_i$, with $a > 0$ for counter-rotation and $a < 0$ for co-rotation. Alternatively to the rotation ratio one can also use the inverse Rossby number

$$Ro^{-1} = \frac{2\omega_o d}{|\omega_i - \omega_o| r_i} = -2 \frac{1 - \eta}{\eta} \frac{a}{|1 + a|}. \quad (3)$$

The advantage of this representation is that in the coordinate system co-rotating with the outer cylinder, Ro^{-1} directly characterises the strength of the driving Coriolis force, as can be seen from the underlying Navier-Stokes equation formulated in that coordinate system,

$$\frac{\partial \mathbf{u}}{\partial t} + \mathbf{u} \cdot \nabla \mathbf{u} = -\nabla p + \frac{f(\eta)}{Ta^{1/2}} \nabla^2 \mathbf{u} - Ro^{-1} \mathbf{e}_z \times \mathbf{u}, \quad (4)$$

where $f(\eta) = (1 + \eta)^3 / (8\eta^2)$. The same data of the (Re_o, Re_i) parameter space of figure 3a are shown in figure 3b in the (Ta, Ro^{-1}) parameter space. But as we will see, the representation of the data in terms of Ro^{-1} also has disadvantages, and we will use Ro^{-1} and the (negative) rotation ratio a in parallel.

The advantage of using the Taylor number rather than the Reynolds numbers is that then the analogy between TC flow and RB is illuminated, as worked out in detail in Eckhardt, Grossmann & Lohse (2007b). In that paper it was shown in particular that the conserved transport quantity in TC flow is the angular velocity flux from the inner to the outer cylinder,

$$J^\omega = r^3 \left(\langle u_r \omega \rangle_{A,t} - \nu \partial_r \langle \omega \rangle_{A,t} \right). \quad (5)$$

Here, $u_r(u_\phi)$ is the radial (azimuthal) velocity, $\omega = u_\phi/r$ the angular velocity, and $\langle \dots \rangle_{A,t}$ characterizes averaging over time and the area with constant distance from the axis. In analogy to the definition of the dimensionless heat flux in RB flow, Eckhardt, Grossmann & Lohse (2007b) defined a ‘‘Nusselt number’’ as the ratio of the angular velocity flux J^ω and its value $J_{lam}^\omega = 2\nu r_i^2 r_o^2 (\omega_i - \omega_o) / (r_o^2 - r_i^2)$ for the laminar case, i.e.

$$Nu_\omega = J^\omega / J_{lam}^\omega. \quad (6)$$

Nu_ω is the key response parameter of the TC system. It is directly connected to the torque τ that is necessary to keep the angular velocities constant. Its dimensionless form is defined as

$$G = \frac{\tau}{2\pi \ell \rho \nu^2} = Nu_\omega \frac{J_{lam}^\omega}{\nu^2} = Nu_\omega G_{lam}. \quad (7)$$

Here ℓ is the height of the part of the cylinder on which the torque is measured, ρ the density of the fluid, and G_{lam} is the dimensionless torque for the laminar case. Also Dubrulle & Hersant (2002) worked out the analogy between TC and RB flow, but still used the dimensionless torque G as response parameter. Yet another possibility often used to represent the data is the friction coefficient $c_f = ((1 - \eta)^2 / \pi) G / Re_i^2$ (Lathrop, Fineberg & Swinney 1992a).

The second key response parameter is the degree of turbulence of the *wind* in the gap of the cylinders, which measures the strength of the secondary flows – the r - and z -components of the velocity field (u_r and u_z). Since the time-averaged wind velocity is generally very small when the secondary flows are not stable over time – i.e. $\langle u_r \rangle \simeq 0$ and $\langle u_\phi \rangle \simeq 0$ – the standard deviation of the wind velocity is used to quantify the wind Reynolds number,

$$Re_w = \frac{\sigma_{u_w}(r_o - r_i)}{\nu}. \quad (8)$$

σ_{u_w} can be chosen to be the standard deviation of either the radial or axial velocity.

The key issue now is to understand how the response parameters Nu_ω and Re_w depend on the control parameters Ta , Ro^{-1} , and η .

3. General flow features with increasing driving strength

Before we answer this question in section 4, we will first report the changes in the general flow features with increasing degree of turbulence. A good overview is obtained from the direct numerical simulations (DNS) of the Navier-Stokes equation of Ostilla-Mónico et al. (2014c), who significantly extended the parameter space of Andereck, Liu & Swinney (1986) (figure 2) towards much larger Reynolds numbers (up to 10^5), as shown via phase diagrams in both the (Re_o, Re_i) and the (Ta, Ro^{-1}) representation in figure 4. Note that the whole phase diagram of figure 2 with all its rich structure fits into a dot-like region in the representations of figure 4b, whereas in the logarithmic representation of figure 4a it appears in the very left part for small $Ta \lesssim 10^6$ as “lam TRs”, “lam TRs at IC”, and of course as “Rayleigh stable”.

At Taylor numbers that are still low ($Ta \sim 10^6$, see figure 5a), the gap between the cylinders is filled with coherent structures (‘Taylor rolls’, also called ‘Taylor vortices’)(see e.g. the reviews by DiPrima & Swinney 1981; Tagg 1994; Fardin, Perge & Taberlet 2014), whose length scale decreases with increasing Ta . Around $Ta \approx 3 \times 10^6$ (in the Rayleigh unstable regime) the coherence length of the structures becomes smaller than the characteristic integral length scale (the gap width d) and turbulence starts to develop in the bulk at length scales between the inner (connected to the Kolmogorov scale) and the outer length scale d . At the same time boundary layers (BLs) start to develop at the inner and outer cylinder, with statistical properties that differ to the bulk flow. The boundary layers are still of laminar type, which – in spite of time dependence – can be described by the Prandtl-Blasius theory. In analogy to RB flow we call this regime – with a turbulent bulk and boundary layers of Prandtl-Blasius type – the *classical regime* of TC turbulence. A snapshot of the angular velocity profile in this regime is shown in figure 5b. In the turbulent bulk, depending on Ro^{-1} , either the Taylor rolls survive, or they partly survive close to the inner cylinder, or else the bulk is featureless, see figure 4a and the detailed discussion in section 5.

However, around $Ta^* \simeq 3 \times 10^8$ (for $\eta = 0.71$) the situation changes drastically, as then the boundary layers are sheared strongly enough to undergo a shear instability and

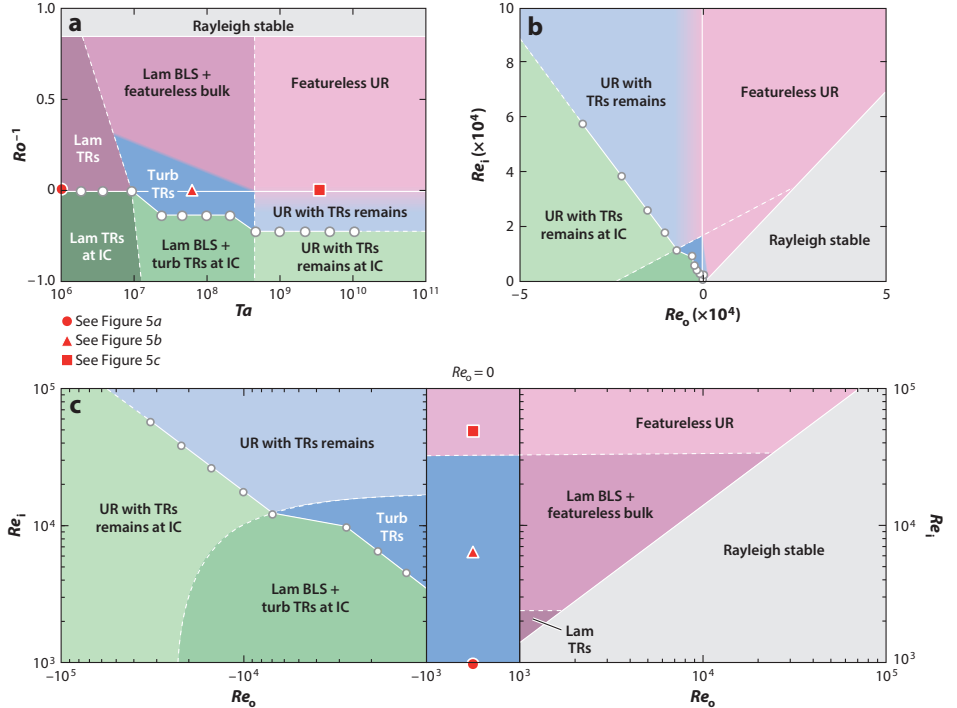


Figure 4

Different regimes in the (Ta, Ro^{-1}) (top-left) and (Re_o, Re_i) (top-right and bottom) phase spaces for $\eta = 0.714$, as obtained from the direct numerical simulations of Ostilla-Mónico et al. (2014c). The hollow circles indicate the location of optimal transport, and serve as an indication of the location of the borderline between the co-rotating or slowly counter-rotating regime (CWCR, blueish and reddish) and the strongly counter-rotating regime (SCR, greenish). Abbreviations: boundary layer (BL), Taylor rolls (TR), ultimate regime (UR), and inner cylinder (IC). Figures taken from Ostilla-Mónico et al. (2014c). The red dot, triangle, and square correspond to the locations of the three cases shown in figure 5.

become turbulent, i.e., of Prandtl-von Kármán type. A snapshot of this regime is shown in figure 5c. This regime is called the *ultimate regime* of TC turbulence, again in analogy to the ultimate regime in RB flow (Kraichnan 1962; Ahlers, Grossmann & Lohse 2009; Grossmann & Lohse 2011). The typical characteristic of the turbulent boundary layer is the approximately logarithmic velocity profile, as will be discussed in section 5. Note that at this transition, the bulk flow does not change much: Depending on Ro^{-1} , it is still either featureless (for positive Ro^{-1} meaning co-rotation) or features Taylor rolls – either over the full bulk area (the gap width minus the boundary layers) or, due to the stabilisation by strong counter-rotation of the outer cylinder, only close to the inner cylinder; again see figure 4. In addition, the statistics of the turbulent fluctuations in the bulk change only quantitatively beyond the transition towards the ultimate regime, with the inertial regime increasing in size.

The separation of the flow domain into bulk and BLs is analogous to the situation in RB

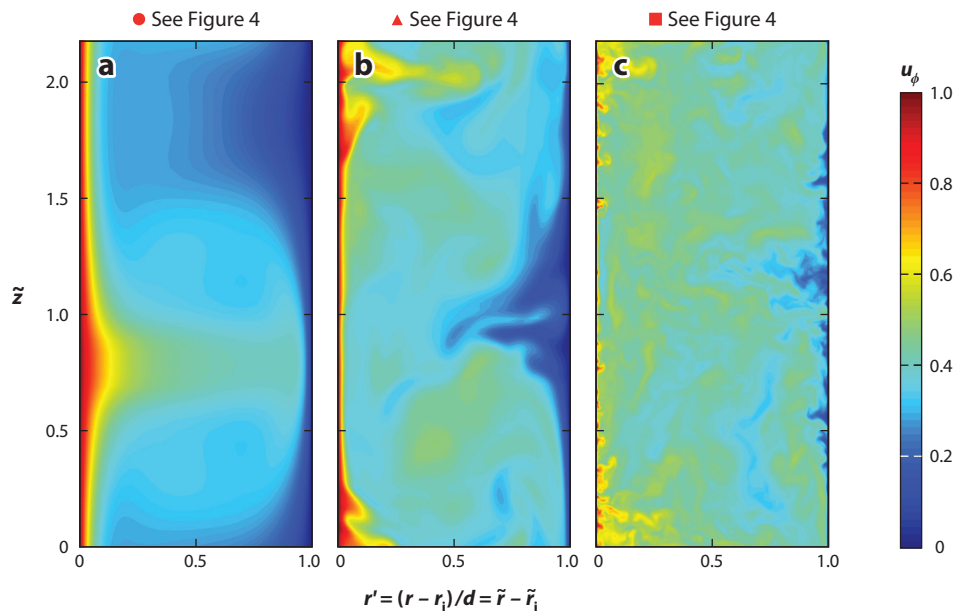


Figure 5

Snapshots of the angular velocity for pure inner cylinder rotation $Ro^{-1} = 0$ and $\eta = 0.714$ as obtained from the DNS of Ostilla-Mónico et al. (2014b). Periodic boundary conditions in axial direction were used and $\tilde{r} = r/d$ and $\tilde{z} = z/d$. (a) $Ta = 7 \times 10^5$ (the red dot in figure 4, laminar Taylor rolls), (b) $Ta = 5 \times 10^7$ (the red triangle in figure 4, classical regime with BLs of Prandtl-Blasius type and a turbulent bulk with Taylor rolls), (c) $Ta = 4 \times 10^9$ (the red square in figure 4, ultimate regime with turbulent BLs and a featureless turbulent bulk).

flow. Therefore the unifying scaling theory developed by Grossmann & Lohse (2000, 2001, 2002, 2004) for RB flow is also applicable here. This was done by Eckhardt, Grossmann & Lohse (2007b). Here we only note that this also holds for the transition to the ultimate regime and for the ultimate regime itself, both for the scaling of Nu_ω and for the profiles (Grossmann & Lohse 2011, 2012; Grossmann, Lohse & Sun 2014), as we will elaborate in the next two sections.

There is, however, a quantitative difference: In RB flow the shear instability of the kinetic boundary layer is only indirectly induced by the thermal driving; namely, the driving first induces a large scale wind, which then in turn builds up the shear near the boundaries. The Ra range in the classical state is very wide (Ra from 10^7 to 10^{14}), and the system only enters into the ultimate state at extremely high Ra number ($Ra^* \simeq 10^{14}$ for Prandtl number ~ 1) that results in many challenges for experiments and numerics (Ahlers, Grossmann & Lohse 2009). Though numerous efforts have been put forward to reach this critical Rayleigh number Ra^* in order to study the ultimate RB turbulence, only very few experiments reach this value, e.g. those of He et al. (2012b,a); Roche et al. (2010); Ahlers, Bodenschatz & He (2014).

In contrast, in TC flow the driving is directly through the rotating cylinders, giving rise to very large shear directly. Since the shear driving in TC flow is much more efficient

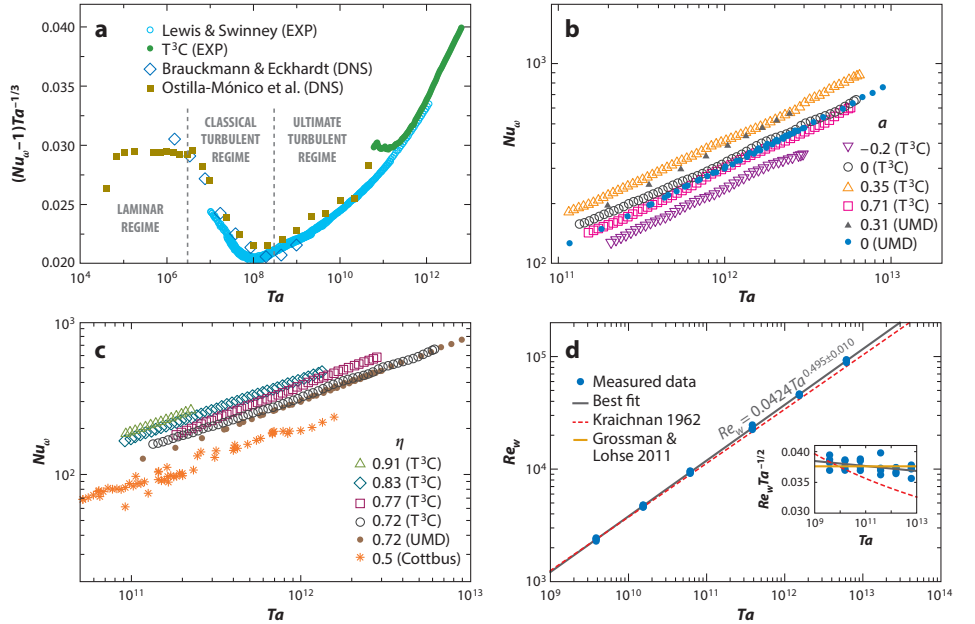


Figure 6

(a) Compensated Nu_w vs. Ta for $\eta = 0.71$ – 0.72 . The data are from experiments ($\eta = 0.72$) by Lewis & Swinney (1999) and van Gils et al. (2012) (T³C) and numerical simulations ($\eta = 0.71$) by Brauckmann & Eckhardt (2013a) and Ostilla-Mónico et al. (2014b). Figure taken from Ostilla-Mónico et al. (2014b). (b) Nu_w vs. Ta at various rotation ratios a , measured in two different facilities for $\eta \simeq 0.72$: T³C - data measured in the Twente Turbulent Taylor-Couette facility (van Gils et al. 2011b, 2012), UMD - data measured in the Maryland TC facility (Paoletti & Lathrop 2011). (c) The measured data on Nu_w vs. Ta for only inner cylinder rotation ($a = 0$) at various radius ratios η : T³C - data measured in the Twente Turbulent Taylor-Couette facility (van Gils et al. 2011b, 2012), UMD - data measured in the Maryland TC facility (Paoletti & Lathrop 2011), Cottbus - data measured in the Cottbus TC facility (Merbold, Brauckmann & Egbers 2013). (d) The wind Reynolds number Re_w vs. Ta . The data measured at midheight in the T³C facility are shown as separate blue dots, showing the quality of the reproducibility and the statistical stationarity of the measurements. The straight line is the best fit $Re_w = 0.0424Ta^{0.495 \pm 0.010}$ and the red dashed line is the Kraichnan (1962) prediction. The inset shows the compensated plot $Re_w/Ta^{1/2}$ vs. Ta . The horizontal green line is the prediction by Grossmann & Lohse (2011). Figure taken from Huisman et al. (2012).

than the indirect driving by heating in RB flow, the TC flow enters the ultimate regime at a much lower $Ta^* \simeq 3 \times 10^8$ (for $\eta = 0.71$). Therefore it is an ideal system to study turbulent flow in the ultimate regime at a wide Ta regime (10^8 to 10^{13} , the latter of which is what presently can be achieved in the T³C setup). In the next section, we will focus on the dependence of Nu_w on the control parameters (Ta , a , and η) in both the classical (up to $Ta^* \simeq 3 \times 10^8$) and the ultimate regime (beyond $Ta \gg 3 \times 10^8$).

4. Global response of the TC system: Nu_w and Re_w

The transitions between the different regimes in the phase space are reflected in the global responses of the system. In this section we will discuss these dependences one for one.

4.1. Nu_w and Re_w vs. Ta

The most relevant dependence may be that of Nu_w on Ta . In a log-log plot of these quantities it is hard to recognize the transitions. They become much more visible in so-called *compensated* plots such as shown in figure 6a, in which $(Nu_w - 1)/Ta^{1/3}$ is plotted vs. Ta , for pure inner cylinder rotation $a = 0$, for radius ratios η between 0.71 and 0.72, and for $10^4 < Ta < 10^{13}$. By plotting the data in this compensated way (i) the laminar case $Nu_w = 1$ is subtracted and (ii) one focuses on the differences between the scaling exponents of the classical regime (where for $a = 0$ it is $\leq 1/3$) and the ultimate regime (where in general it is larger than $1/3$, but $\leq 1/2$, which is the theoretical upper bound (Howard 1972; Doering & Constantin 1994)). As seen from figure 6a, the experimental and numerical data originating from two different experimental setups and two different DNS codes agree very well: After the onset of Taylor vortices at $Ta \simeq 10^4$ and up to $Ta \simeq 3 \times 10^6$, one observes the scaling law $Nu_w - 1 \sim Ta^{1/3}$ for the pure laminar regime. Then the flow becomes time-dependent and for $3 \times 10^6 \lesssim Ta \lesssim 3 \times 10^8$ the effective scaling $Nu_w \sim Ta^\gamma$ with $\gamma < 1/3$ of the classical turbulent state is found, in correspondence with the classical effective $Nu \sim Ra^\gamma$ scaling in RB turbulence (Ahlers, Grossmann & Lohse 2009). In this regime turbulence starts to develop in the bulk of the gap, whereas the BLs still remain of laminar type. At some transitional Taylor number Ta^* , which depends on η and which for $\eta = 0.71$ is $Ta^* \simeq 3 \times 10^8$, the BLs also become turbulent and the flow undergoes a transition to the ultimate regime with an effective exponent $\gamma > 1/3$. In fact, in the Ta range of 10^{11} to 10^{13} , the effective exponent γ is about 0.39 ± 0.02 , which in this regime is consistent with the theoretical prediction of $Nu_w \sim Ta^{1/2} \times \log$ -corrections by Kraichnan (1962) and by Grossmann & Lohse (2011). Such log-correction predictions are typical for logarithmic BLs. Here they were originally derived for RB flow, but can straightforwardly be translated to TC flow based on the analogies between the two systems.

How does the scaling change for co- or counter-rotation, i.e., $a \neq 0$, (but fixed $\eta = 0.72$)? Figure 6b shows $Nu_w(Ta)$ measured in two different TC facilities for various a . These measurements suggest that the scaling exponent γ of $Nu_w \sim Ta^\gamma$ has a weak dependence on a in the Rayleigh unstable regime. And what is the dependence on the radius ratio η ? Figure 6c displays Nu_w vs. Ta at $a = 0$ for various η for three different TC facilities. Again the scaling exponent γ seems to vary only weakly. In summary, for all examined a and η values, the scaling exponent γ is found to be about 0.39 ± 0.03 for $10^{11} \leq Ta \leq 10^{13}$.

What about the corresponding scaling of the wind Reynolds number? For the ultimate regime (originally in RB flow) Kraichnan (1962) had derived log-corrections as well, namely $Re_w \sim Ta^{1/2} (\log Ta)^{-1/2}$. In contrast, Grossmann & Lohse (2011) derived a different prediction: the logarithmic corrections due to the viscous (wind) boundary layer and the thermal (azimuthal velocity in TC) boundary layer remarkably cancel out, resulting in the scaling $Re_w \sim Ta^{1/2}$, without any logarithmic corrections. Using high-speed Particle Image Velocimetry (PIV), Huisman et al. (2012) directly measured the radial velocity fluctuations and extracted the wind Reynolds number as $Re_w = \sigma_{u_r}(r_o - r_i)/\nu$, where σ_{u_r} is the standard deviation of the radial velocity. The measurements shown in figure 6d reveal a clear scaling of the wind Reynolds number with the Taylor number, $Re_w \sim Ta^{0.495 \pm 0.010}$, which

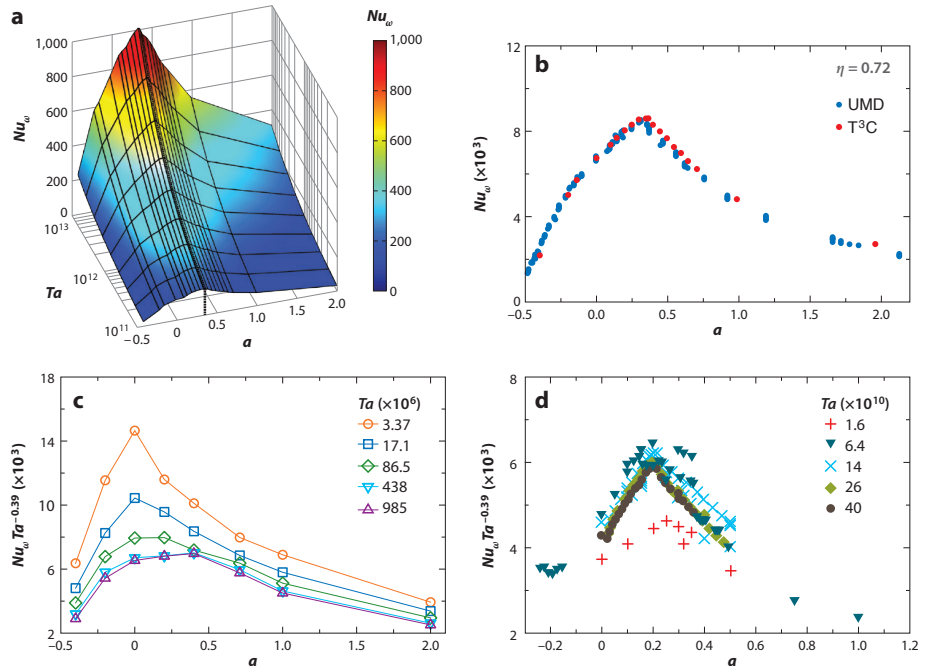


Figure 7

(a) Three-dimensional (interpolated and extrapolated) overview $Nu_\omega(Ta, a)$ of the experimental results by van Gils et al. (2012). The color and the height correspond to the Nu_ω value. Figure taken from van Gils et al. (2012). (b) The compensated $Nu_\omega/Ta^{0.39}$ vs. a for the data measured in two different experimental facilities, i.e. T³C (van Gils et al. 2011b, 2012) and Maryland (Paoletti & Lathrop 2011). The two data sets show excellent agreement. (c) Numerical data: $Nu_\omega/Ta^{0.39}$ versus rotation ratio a for varying Ta numbers at $\eta = 0.5$. Figure taken from Brauckmann & Eckhardt (2013a) with permission from the authors. (d) Experimental data: $Nu_\omega/Ta^{0.39}$ versus rotation ratio a for varying Ta numbers at $\eta = 0.5$. Figure taken from Merbold, Brauckmann & Egbers (2013) with permission from the authors.

is consistent with the prediction by Grossmann & Lohse (2011).

4.2. Nu_ω vs. a or vs. Ro^{-1}

From figure 6b we have seen that the rotation ratio a hardly affects the *scaling* of Nu_ω vs. Ta . However, this is very different for the *absolute value* of Nu_ω , which does depend on a . Figure 7a gives a three-dimensional representation of the measured full dependence $Nu_\omega(Ta, a)$, clearly revealing a non-monotonic dependence of Nu_ω on a with a pronounced maximum at $a_{opt} = 0.33 \pm 0.03$ (for the radius ratio $\eta = 0.72$ of that specific experiment and for large enough Ta), very different from $a = 0$. This pronounced maximum of Nu_ω – also clearly seen in the projection figure 7b – reflects the optimal angular velocity transport from the inner to the outer cylinder at this angular velocity ratio. The positions of the maxima in the (Ta, Ro^{-1}) and (Re_o, Re_i) parameter spaces is marked as a connected line

of white circles, see figure 4. For the given radius ratio $a_{opt} = 0.33 \pm 0.03$ corresponds to $Ro_{opt}^{-1} = -0.20 \pm 0.02$. Intuitively, one might have expected that $Nu_\omega(Ta, Ro^{-1})$ has its maximum at $Ro^{-1} = 0$, i.e. $\omega_o = 0$ (pure inner cylinder rotation), since outer cylinder rotation stabilizes an increasing part of the flow volume for increasing counter-rotation rate. This indeed is the case for small $Ta \lesssim 10^7$, as seen from fig. 4 and fig. 7c, but for larger Ta weak counter-rotation ($0 < Ro^{-1} < Ro_{opt}^{-1}$) can further enhance the angular velocity transport through intermittent turbulent bursts from the BLs (van Gils et al. 2012), though the flow is predominantly Rayleigh-stable near the outer cylinder. Following Ostilla-Mónico et al. (2014c), we call the regime above the line of the maxima Ro_{opt}^{-1} in the parameter spaces of figure 4 the co-rotating or weakly counter-rotating regime (CWCR, shaded blueish and reddish in that figure). A reduction of the angular velocity transport only sets in below this line, in what we call the strongly counter-rotating regime (SCR, greenish). In general, the line of the maxima in parameter space reflects the competition of destabilization by the inner cylinder rotation and stabilization by the outer cylinder rotation. This competition depends on the radius ratio η , as seen from figures 7c,d, in which the angular velocity transport as measured by Merbold, Brauckmann & Egbers (2013) for $\eta = 0.5$ is shown, displaying a maximum around $a_{opt} = 0.20$ to 0.25 for large enough Ta , corresponding to $Ro_{opt}^{-1} = -0.33$ to -0.4 .

Note that in figures 7b-d we have compensated Nu_ω with $Ta^{0.39}$. This is the mean effective scaling of Nu_ω in the explored large Ta number regime (10^9 to 10^{13}), in which $Nu_\omega(Ta, Ro^{-1}, \eta)$ factorizes into $Nu_\omega(Ta, Ro^{-1}, \eta) \sim Ta^{0.39} f(Ro^{-1}, \eta)$ or $Nu_\omega(Ta, a, \eta) \sim Ta^{0.39} f(a, \eta)$. In section 5 we will explain the dependence of the scaling function f on Ro^{-1} and η .

4.3. Nu_ω vs. η

We finally report the radius ratio dependence of Nu_ω in more detail. Figure 8a shows $Nu_\omega/Ta^{0.39}$ as function of a for varying values of η from 0.5 to 0.909. Nu_ω increases with increasing η in the present parameter regime, indicating that the angular velocity transport is more efficient for a larger radius ratio η . As seen in figure 8a, the shapes of the curves $Nu_\omega/Ta^{0.39}$ vs. a depend strongly on η : the peak is very narrow and pronounced at low radius ratios, and the location of a_{opt} for the optimal transport can be easily identified. In contrast, for larger radius ratios the peak of the curve becomes less steep. This suggests that the angular velocity ratio of optimal transport a_{opt} becomes less sharply defined as the radius ratio η approaches 1. As can be seen from figure 8a, it is very difficult to precisely identify the location of a_{opt} for $\eta = 0.909$, since the curve is almost flat for the data of $\eta = 0.909$ at $a < 0.5$.

From the curves in figure 8a, we can identify a_{opt} as a function of η , which is plotted in figure 8b. These data assemble the state-of-the-art results on the optimal transport in high-Reynolds number TC flows. Overall, a_{opt} increases with increasing η for $\eta \lesssim 0.8$, and it seems to saturate at higher η .

The same data $Nu_\omega(a)$ in figure 8a are shown in the $Nu_\omega(Ro^{-1})$ representation in figure 8c, seemingly exhibiting a different trend: the steepness of the peak does not depend much on the radius ratio η . This difference in the trends in figure 8a and figure 8c is due to the transformation between the control parameters a and Ro^{-1} (eq. 3). As we know, Ro^{-1} takes its justification as control parameter directly from the Navier-Stokes equations, in which it characterises the strength of the Coriolis force. However, it is hard to compare

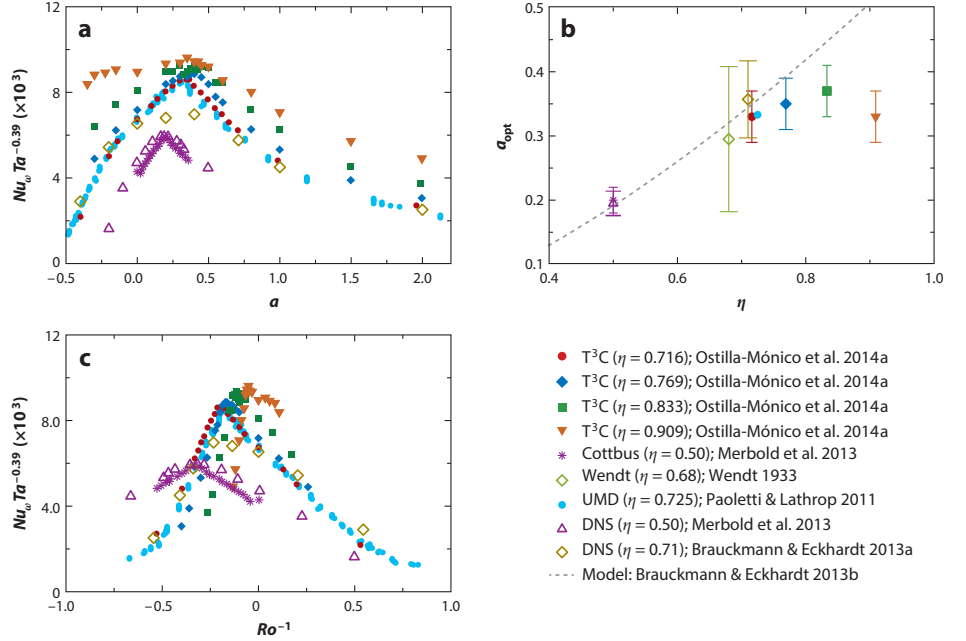


Figure 8

Radius ratio η -dependence of Nu_ω : Plots of $Nu_\omega/Ta^{0.39}$ versus (a) a and versus (c) Ro^{-1} from the collection of state-of-the-art data at various η . (b) a_{opt} obtained from figure (a) versus η . Symbols represent experimental and numerical results; the model prediction of Brauckmann & Eckhardt (2013b) is plotted as dashed line. Figure taken from Ostilla-Mónico et al. (2014a).

the data of $Nu_\omega(Ro^{-1})$ for different η , because Ro is defined as the ratio of shear rate ($(\omega_i - \omega_o)/d$) and solid-body rotation (ω_o/r_i), which involve two different length scales, i.e. d and r_i .

We finally also note that the transitional Taylor number Ta^* to the ultimate state is larger at smaller radius ratios, e.g., $Ta^* \simeq 10^{10}$ for $\eta = 0.5$ (Ostilla-Mónico et al. 2014c).

5. Local flow organization: Profiles, rolls, and optimal transport

After the general overview of the flow organization in section 3 and after having reported the global flow response in section 4, we will now look into the profiles and into the detailed flow organization. This will also allow us to rationalize the dependence $f(Ro^{-1}, \eta)$ of the global transport properties reported above.

5.1. Profiles

For Taylor numbers below the threshold $Ta_c \approx 10^4$ for the onset of instabilities, the angular velocity profile in TC flow follows the classical non-vortical laminar profile (see e.g. Landau

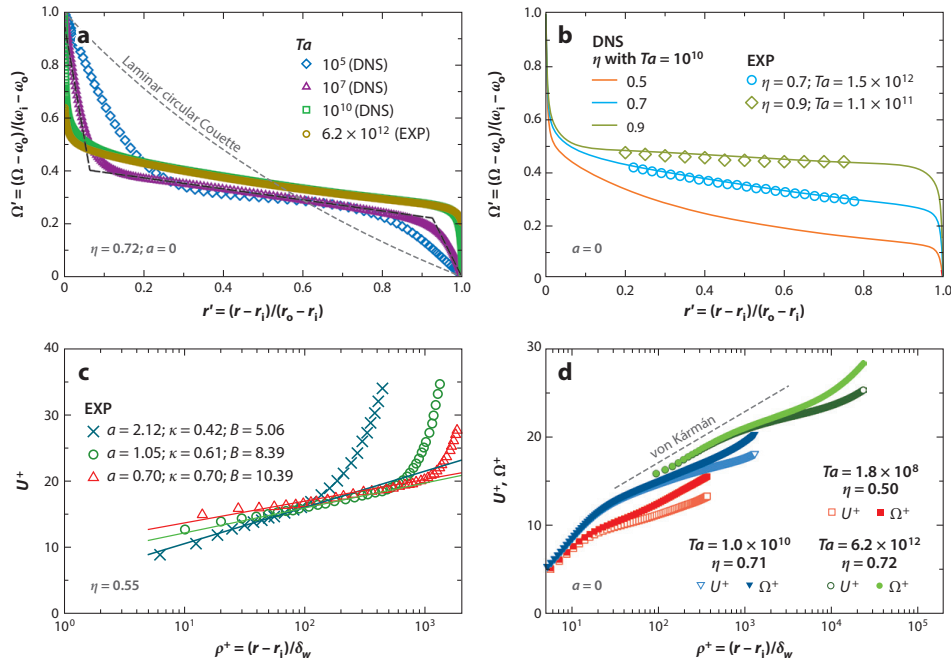


Figure 9

(a) Angular velocity profiles for varying Taylor numbers across the TC gap for only inner cylinder rotation at $\eta = 0.71$ (DNS) and 0.72 (experiments). The black line represents the exact laminar circular-Couette (nonvortical) solution of the Navier-Stokes equations. Figure adapted from Huisman et al. (2013). (b) Angular velocity profiles for varying radius ratio across the TC gap for only inner cylinder rotation. The lines are the results from numerical simulations and the symbols represent the experimental data. Figure taken from Ostilla-Mónico et al. (2014a). (c) The inner cylinder azimuthal velocity profile in wall units vs. the radial distance from the wall (again in wall units) at varying rotation ratios. Here $\eta = 0.55$ and the Taylor numbers are 4.9×10^9 ($a=2.12$), 7.3×10^9 ($a=1.05$), and 1.1×10^{10} ($a=0.70$), respectively. Figure taken from van Hout & Katz (2011) with permission from the authors. (d) A log-linear plot of the inner cylinder azimuthal velocity profiles (U^+) and angular velocity profiles (Ω^+) near the inner cylinder in so-called wall units. Experimental data at $Ta = 6.2 \times 10^{12}$ are taken from Huisman et al. (2013), the numerical data at $Ta = 1.0 \times 10^{10}$ from Ostilla-Mónico et al. (2014b), and the numerical data at $Ta = 1.8 \times 10^8$ from Chouippe et al. (2014) with permission from the authors. The radial distance from the inner cylinder wall is normalized by the wall unit, i.e. $\rho^+ = (r - r_i)/\delta_{w,i}$, where $\delta_{w,i}$ is the viscous length scale for the inner cylinder boundary layer.

& Lifshitz 1987),

$$\Omega_{\phi,\text{lam}}(r) = A + B/r^2, \quad A = \frac{\omega_o - \eta^2 \omega_i}{1 - \eta^2}, \quad B = \frac{(\omega_i - \omega_o)r_i^2}{1 - \eta^2}. \quad (9)$$

For larger Ta the flow becomes time dependent and then $\Omega(r) = \langle \omega(r) \rangle_t$ is the time-averaged angular velocity. This profile is shown as the black line in figure 9a (for $\eta = 0.7$), in the representation $\Omega' = (\Omega(r) - \omega_o)/(\omega_i - \omega_o)$ vs. $r' = (r - r_o)/(r_i - r_o)$. With increasing Ta number, the profiles start to deviate from the non-vortical laminar one, as also shown

in figure 9a (for the case of zero outer cylinder rotation, $Ro^{-1} = 0$). After the onset of Taylor vortices, eventually time dependences set in and the large-scale coherent structures break up into smaller structures. Finally, the separation between the bulk and the BLs starts to develop. As seen from figures 5a,b and 9a, between $Ta = 10^5$ and 10^7 the profiles can be decomposed into a bulk and two boundary layers. The boundary layers can be well characterized by the Prandtl-Blasius BL theory for BLs of laminar type, as illustrated by the dashed lines in the figure. With further increase of Ta , the BLs become increasingly thin and around $Ta^* \simeq 3 \times 10^8$ finally undergo a transition to turbulent BLs of Prandtl-von Kármán type, see figure 5c. In figure 9a we show the angular velocity profiles at $Ta = 10^{10}$ and 6.2×10^{12} , both clearly being of turbulent type with a logarithmic shape, as we will see later.

The angular velocity profile also strongly depends on the radius ratio η , as seen from the experimental and DNS data in figure 9b. The angular velocity gradient in the bulk decreases with increasing η , and the profile is almost flat in the bulk for $\eta = 0.9$. In contrast, for small $\eta = 0.5$ a large decrease of Ω' to values $\ll 0.5$ (i.e., the value in the limiting case $\eta = 1$, plane Couette flow) is observed, coinciding with a considerable angular velocity gradient.

In the ultimate state of TC turbulence, the velocity boundary layer is turbulent and the profile was believed to be described by the law of the wall suggested by Prandtl and von Kármán,

$$U_\phi^+(\rho^+) = \kappa^{-1} \log \rho^+ + B. \quad (10)$$

Here κ is a generalized von Kármán constant and $\rho = r - r_i$ or $\rho = r_o - r$ are the distances from the wall, presented in the usual wall units $\rho^+ = (r - r_i)/\delta_{w,i}$ or $\rho^+ = (r_o - r)/\delta_{w,o}$, just as $U_\phi^+ = U_\phi/u_{\tau,(i,o)}$, with $\delta_{w,(i,o)} = \nu/u_{\tau,(i,o)}$ and $u_{\tau,(i,o)} = \sqrt{\tau_{(i,o)}/\rho}$. Since the angular velocity flux is conserved in the radial direction, the wall units for the outer boundary layer are directly connected to the inner ones: $u_{\tau,i}/u_{\tau,o} = 1/\eta$, and $\delta_{w,i}/\delta_{w,o} = \eta$. In this representation the von Kármán constants κ were found to depend on Ta and on the rotation ratio a , as shown in figure 9c taken from van Hout & Katz (2011).

Recent work by Grossmann, Lohse & Sun (2014) based on the Navier-Stokes equations suggests that the log-law is more appropriate for the *angular* velocity Ω rather than for the *azimuthal* velocity U_ϕ , i.e.,

$$\Omega^+(\rho^+) = \kappa^{-1} \log \rho^+ + B, \quad (11)$$

with $\Omega^+(\rho^+) \equiv (\omega_{i,o} - \Omega(\rho^+))/\omega_{i,o}^*$ and $\omega_{i,o}^* = u_{i,o}/r_{i,o}$ for the inner (outer) cylinder boundary layer. The difference between the angular velocity and the azimuthal velocity profiles is due to the curvature. As shown in figure 9d, for $\eta = 0.71 - 0.72$ this difference only becomes notable for large wall distances near the middle of the TC gap. In contrast, for smaller radius ratio $\eta = 0.50$, the difference between the angular velocity and azimuthal velocity profiles is larger, due to a relatively smaller r_i as shown in figure 9d. For the largest $Ta = 6.2 \times 10^{12}$, the angular velocity profile at ρ^+ between 100 and 1000 roughly follows the Prandtl-von Kármán log-law, with even the same von Kármán constant $\kappa \approx 0.4$ as found for other wall-bounded turbulent flows (Smits, McKeon & Marusic 2010; Smits & Marusic 2013). For lower Ta numbers the von Kármán constant κ in eq. (11) is found to be larger than 0.4 (Huisman et al. 2013; Ostilla-Mónico et al. 2014b), presumably since for these values the turbulent boundary layers are not yet fully developed and due to curvature.

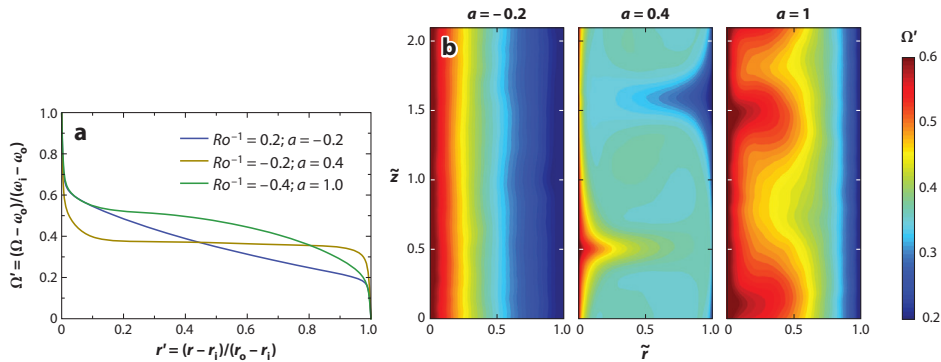


Figure 10

(a) Axially averaged angular velocity profiles at three values of Ro^{-1} (or a) for $\eta = 0.71$ and $Ta = 10^{10}$. (b) Contour plots of the azimuthally- and time-averaged angular velocity field for $Ta = 10^{10}$, $\eta = 0.71$ and three values of Ro^{-1} . The left panel corresponds to $Ro^{-1} = 0.2$ ($a = -0.2$) (CWCR regime) and shows no traces of axial dependence. Plumes detach rapidly into the bulk, where they strongly mix, and thus cannot form large-scale structures. The middle panel corresponds to $Ro^{-1} = -0.22$ ($a = 0.4$). The reduced plume mixing enables the formation of large-scale structures, and a strong signature of them can be seen in the averaged angular velocity field. The right panel corresponds to $Ro^{-1} = -0.4$ ($a = 1$) (SCR regime) and also shows some signatures of large-scale structures. However, these do not fully penetrate the gap but stop at the border to the Rayleigh-stable zones near the outer cylinder. Figures taken from Ostilla-Mónico et al. (2014c).

5.2. Rotation ratio dependence of profiles and optimal transport

We now describe in more detail how the profiles depend on the rotation ratio a (or alternatively on the strength of the Coriolis force $\propto Ro^{-1}$). As seen from figure 10, the angular velocity profile and flow structures in the bulk indeed strongly depend on this parameter, highlighting the effect of the Coriolis force on the flow organization. Depending on Ro^{-1} (or a), we had already defined two regimes in section 3, namely for $Ro^{-1} > Ro_{opt}^{-1}$ a co- and weakly counter-rotating regime (CWCR) and for $Ro^{-1} < Ro_{opt}^{-1}$ a strongly counter-rotating regime (SCR). The transition between these two regimes occurs at the value Ro_{opt}^{-1} (or a_{opt}) of the rotation ratio for which $Nu_{\omega}(Ro^{-1})$ is maximum.

In the CWCR regime the Coriolis force in the Navier-Stokes equation (4) is balanced by the bulk gradient of Ω , which results in a linear relationship between Ro^{-1} and $\partial_r \Omega$ (Ostilla-Mónico et al. 2013). Here $\Omega = \langle \bar{\omega} \rangle_{z,t}$ is time-, axially-, and azimuthally-averaged angular velocity. As shown with the blue line for $a = -0.2$ in figure 10a, the angular velocity gradient in the bulk is large, and to accommodate for this, there is a smaller Ω jump across the boundary layers. In this CWCR regime, the plumes ejected from the boundary layers can be mixed easily in the bulk. As a consequence, the large-scale structures, which essentially consist of unmixed plumes, vanish when the driving is strong enough, see e.g. figure 10 at $a = -0.2$ and $Ta = 10^{10}$.

Beyond the maximum the system enters the SCR regime, i.e., the outer cylinder strongly counter-rotates and generates a Coriolis force which exceeds what the Ω -gradient can balance, i.e. $Ro^{-1} < Ro_{opt}^{-1}$ or $a > a_{opt}$. The threshold value of the rotation ratio for the

transition from the CWCR regime to the SCR regime corresponds to a flat Ω profile (van Gils et al. 2012; Ostilla-Mónico et al. 2014c), as shown with the red line in figure 10a. This flat angular velocity profile in the bulk perfectly resembles RB turbulence for which, due to the absence of a mean temperature gradient in the bulk, the whole heat transport is conveyed by the convective term (Ahlers, Grossmann & Lohse 2009). Thanks to the flat angular velocity profile in the bulk, there is a large Ω jump across the boundary layers, and thus plumes detach violently from the boundary layers, strongly driving the large-scale structures. Therefore, strong large-scale structures form at $a = a_{opt}$, as shown in the middle panel of figure 10b, and these strong mean circulations can be related to the optimum in angular velocity transport Nu_ω (Brauckmann & Eckhardt 2013b; Ostilla-Mónico et al. 2014c). Ostilla-Mónico et al. (2014c) explained also the radius ratio η -dependence of the angular velocity transport with the flat angular velocity profile and the persistence of Taylor rolls: Indeed, $Nu_\omega(\eta)$ seems to have its maximum close to $\eta = 1$ (plane Couette flow), where the angular velocity profile is flat and the rolls are most developed. However, the detailed dependence of $Nu_\omega(\eta)$ around $\eta = 1$ still awaits a detailed numerical and experimental exploration.

In the SCR regime, the vortices cannot fully penetrate the entire domain, due to the insufficient strength of the Coriolis force. Near the outer cylinder, the flow is predominantly Rayleigh-stable. The angular velocity is transported mainly through intermittent turbulent bursts, instead of by convective transport through plumes and vortices (van Gils et al. 2012; Brauckmann & Eckhardt 2013b). In this regime, large-scale coherent rolls cannot develop in the entire gap, as shown in the right panel of figure 10b. Local structures are present only in the zones close to the inner cylinder. The stabilization by the outer rotation is also clearly visible in the angular velocity profile as shown by the green line in figure 10a, in which the outer boundary layer extends deeper into the flow, and the distinction between the bulk and the boundary layer is blurred (Ostilla-Mónico et al. 2014c).

5.3. Multiple turbulent state and their connection to the Taylor rolls

The question is whether the turbulent structures seen in the DNS of Ostilla-Mónico et al. (2014c) up to $Re_{i,o} \sim 10^5$ and marked in the phase diagram fig. 4 survive in TC flows at even higher Reynolds numbers, i.e. $Re_{i,o} \gg 10^5$, beyond what is presently numerically possible. And if so, what is the connection between the turbulent structures and the global angular velocity transport at very high Reynolds numbers?

Fenstermacher, Swinney & Gollub (1979) observed that for increasing Reynolds number the waves on top of the Taylor vortices become increasing complex until only turbulent Taylor vortices are left. Lewis & Swinney (1999) studied the statistics of velocity fluctuations in TC flow for Re_i up to 5×10^5 for pure inner cylinder rotation and found that turbulent Taylor vortices remained at their highest Reynolds number. However, the findings of Lathrop, Fineberg & Swinney (1992a) suggest that for pure inner cylinder rotation the Taylor vortices are not present for Reynolds numbers beyond $Re_i = 1.2 \times 10^5$. As shown in figure 11a,b, the flow structures are visible at $Re_i = 6 \times 10^3$, but seem to have disappeared at $Re_i = 1.22 \times 10^5$.

As discussed above, the flow structures in the bulk, the azimuthal velocity profile and the optimal angular velocity transport are closely connected. To correctly extrapolate to much higher Reynolds numbers it is crucial to know the characteristics of the turbulent state and the possible existence of other such states. Kolmogorov's 1941 paradigm suggests

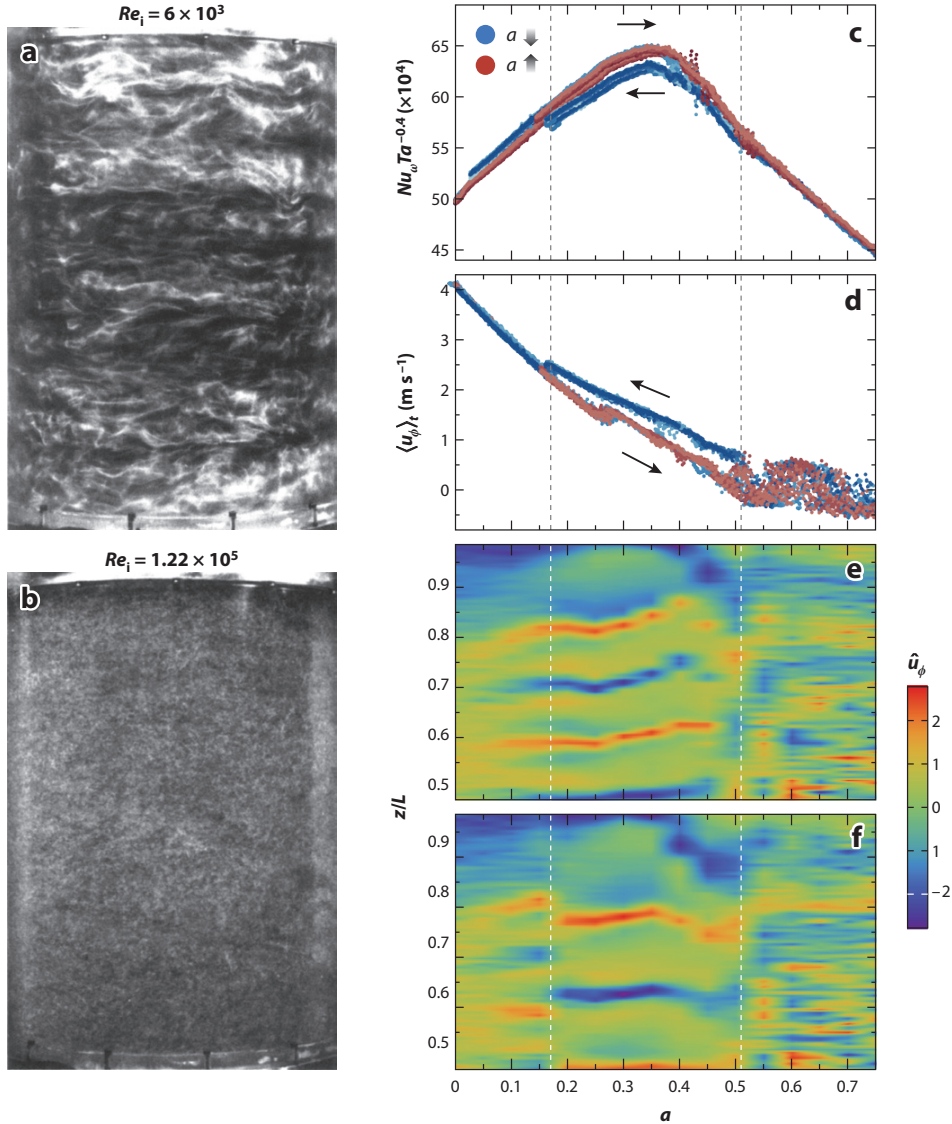


Figure 11

Photographs of flow states at (a) $Re_i = 6 \times 10^3$ and (b) $Re_i = 1.22 \times 10^5$, obtained using Kalliroscope flow visualization. The outer cylinder was stationary for these experiments. Eight vortices are visible in (a) but not in (b). Figures (a,b) taken from Lathrop, Fineberg & Swinney (1992a) with permission from the authors. (c-f) Experimental results measured in the T³C facility at $Ta \approx 10^{12}$. (c) Compensated Nu_w as a function of a . Experiments following trajectories of decreasing a and increasing a are colored in blue and red, respectively. For decreasing a the flow is either in a high or a low state for $0.17 < a < 0.51$, while for increasing a in this regime it always is in the high state. For $a = 0.36$ the Nusselt number of the high state is 2.5% larger than that of the low state. (d) Azimuthal velocity measured at the mid-height and mid-gap as a function of a for trajectories of increasing a and decreasing a . Same colors as in (c). For the local velocity one also sees that the system bifurcates when following the trajectory of decreasing a around $a = 0.51$, choosing either the high or low state for $0.17 < a < 0.51$. (e) and (f) show axial scans of the normalised angular velocity for varying a , following trajectories of increasing a and decreasing a , respectively. One can see the presence of 4 rolls in the top half of the system in (e), while in (f) only 3 rolls are present for $0.17 < a < 0.51$. For $a < 0.17$ and $a > 0.51$ the system is in the same

that for strongly turbulent flows with many degrees of freedom and large fluctuations, there would only be one turbulent state as the large fluctuations would explore the entire higher dimensional phase space. However, recently Huisman et al. (2014) observed conclusive evidence of *multiple* turbulent states for large Reynolds number ($Re_{i,o} \sim 10^6$, $Ta \sim 10^{12}$) TC flow in the regime of ultimate turbulence, by probing the phase space spanned by the rotation rates of the inner and outer cylinder. Furthermore, they found that the optimal transport is directly connected to the existence of large-scale coherent structures.

Figure 11c shows the compensated Nusselt number as a function of a for Huisman et al. (2014)'s measurements with increasing a (red lines) and decreasing a (blue lines). As can be seen, for increasing a (red lines), the torque is continuous and shows a peak around $a = 0.36$, which is similar to the prior observations by van Gils et al. (2011b); Paoletti & Lathrop (2011); van Gils et al. (2012); Merbold, Brauckmann & Egbers (2013). For decreasing a , the torque is found to be same as that with increasing a at $a > 0.51$ and $a < 0.17$. However, for $0.17 < a < 0.51$ the torque is different. For decreasing a the system can enter another state around $a = 0.51$ which is characterized by a lower torque (and thus was called ‘low state’), and around $a = 0.17$ the system sharply jumps back to a higher torque state (‘high state’). Huisman et al. (2014) repeated these experiments to check the reproducibility. For increasing a , the system always goes into the high state, while for decreasing a it goes to the low state (for $0.17 < a < 0.51$) with a high probability (8 out of 10).

To verify that the high and low torque states originate from two different physical flow structures, Huisman et al. (2014) measured the azimuthal velocity at half-height $z = L/2$ and at the center of the gap $r = (r_i + r_o)/2$, as shown in figure 11d. The presence of multiple states in the local measurements of the azimuthal velocity and at the same time the global measurements of the torque clearly indicates that the system can indeed be in different turbulent states, in spite of the very high Taylor number of $\mathcal{O}(10^{12})$ (in the ultimate regime).

In order to further characterize the turbulent state of the system, Huisman et al. (2014) also measured the axial dependence of the azimuthal velocity in the top half of the system at varying a for both the high and the low state. Figure 11e shows the local velocity for the high state with 5 large minima/maxima for $a \leq 0.45$, indicating that 4 turbulent Taylor vortices exist in the top half of the system. For $a \geq 0.5$ the state of the system is less clear, and the system appears to jump between states (without a well-defined a -dependence), as shown in fig. 11e. In the low state, figure 11f shows the same behavior as in the high state of fig. 11e for a outside $[0.17, 0.51]$. However, for $0.17 < a < 0.51$ it is found that the azimuthal velocity has 4 large minima/maxima in the low state, which is the signature of 3 turbulent Taylor vortices in the top half of the system.

It is surprising that multiple turbulent states exist for such large Reynolds number TC flow in the regime of ultimate turbulence. Another striking feature is that the a range, at which the stable (multiple) structures exist, corresponds to the a range for optimal torque transport, reflecting that the optimal transport is connected to the existence of the stable large-scale coherent structures.

6. Flow in the quasi-Keplerian regime

Astrophysical disks are ubiquitous in the universe. These so-called accretion disks can be of two types: the proto-planetary disks and the disks around compact objects such as white dwarfs, neutron stars, and black holes (Ji & Balbus 2013). These disks are supported

almost entirely by the rotation forces, suggesting that the rotating matter follows a law similar to Kepler’s law for planetary motion (Ji & Balbus 2013). The orbiting matter (mostly gas) has to lose its angular momentum in order to move radially inwards into the central object. The observed accretion rates of astrophysical disks cannot be accounted for by the transport of angular momentum resulting from pure molecular viscosity (Schartman, Ji & Burin 2009; Ji & Balbus 2013). Therefore, to account for the observed transport in accretion disks, turbulence has to enter into the problem. Two possible instabilities have been proposed to account for this, namely a magneto-rotational instability (MRI) and a subcritical hydrodynamical instability (SHI).

The latter one is the reason for which the TC system is relevant in this context, as it has been suggested as model system for studying the transport behavior in accretion disks (see e.g. Richard 2001; Dubrulle et al. 2005; Avila 2012; Ji & Balbus 2013). The astrophysical community uses different control and response parameters from those introduced in section 2. More specifically, rather than using the Taylor number Ta (or $Re_{i,o}$) and the rotation ratio a (or the inverse Rossby number Ro^{-1}) as control parameter, that community uses a shear Reynolds number Re_s and the parameter q , which are defined through the relations (Paoletti et al. 2012; Ji et al. 2006)

$$Re_s = \frac{2}{1 + \eta} |\eta Re_o - Re_i|, \quad \omega_i/\omega_o = \eta^{-q}. \quad (12)$$

The q parameter is real for the co-rotating situation, which is the only case we consider in this section. The parameter space at different q values is shown in figure 12a. TC flow with $q > 2$ (discussed in the previous sections) is linearly unstable at sufficiently high Reynolds numbers, due to the centrifugal instability. In the regime $q < 2$, in which the angular momentum Ωr^2 radially increases with increasing r ($\omega_i r_i^2 < \omega_o r_o^2$), the flow is linearly stable according to the Rayleigh criterion (Lord Rayleigh 1917). This includes subrotation ($\omega_i < \omega_o$), solid-body ($\omega_i = \omega_o$), and super-rotation ($\omega_i > \omega_o$). The flow in the region ($\omega_i > \omega_o$ and $\omega_i r_i^2 < \omega_o r_o^2$, i.e., $0 < q < 2$) is often referred to as *quasi-Keplerian flow*, since it includes cylinder rotation rates ($q = 3/2$) obeying Kepler’s law relating orbital radius and period. As response parameter the astrophysical community uses the dimensionless turbulent viscosity β (Richard & Zahn 1999; Dubrulle et al. 2005; F. Hersant, B. Dubrulle & J.-M. Huré 2005) defined through

$$\beta = \frac{2(1 - \eta)^4}{\pi \eta^2} \frac{G}{Re_s^2} = \frac{2(1 - \eta)^4}{\pi \eta^2} \frac{Nu_\omega G_{lam}}{Re_s^2}, \quad (13)$$

rather than the dimensionless torque G or the angular velocity Nu_ω .

The key question now is whether the TC flow in the linearly stable quasi-Keplerian regime ($0 < q < 2$) can nevertheless become unstable to finite size perturbations, due to a subcritical transition to turbulence. Indeed, in spite of linear stability, at large enough Reynolds numbers shear flow *may* get unstable, namely through the so-called non-normal - nonlinear mechanism, as well known from pipe flow or plane Couette flow, see e.g. Trefethen et al. (1993); Grossmann (2000); Eckhardt et al. (2007).

Paoletti & Lathrop (2011) and Paoletti et al. (2012) examined the flow stability by measuring the global torque as a function of Reynolds number using the Maryland TC facility ($\eta = 0.7245$, aspect ratio $\Gamma = 11.47$, measurements of the torque only with the central part of the inner cylinder) in the quasi-Keplerian regime. The axial boundaries (end plates) in their experiments rotated with the outer cylinder. The measured dimensionless

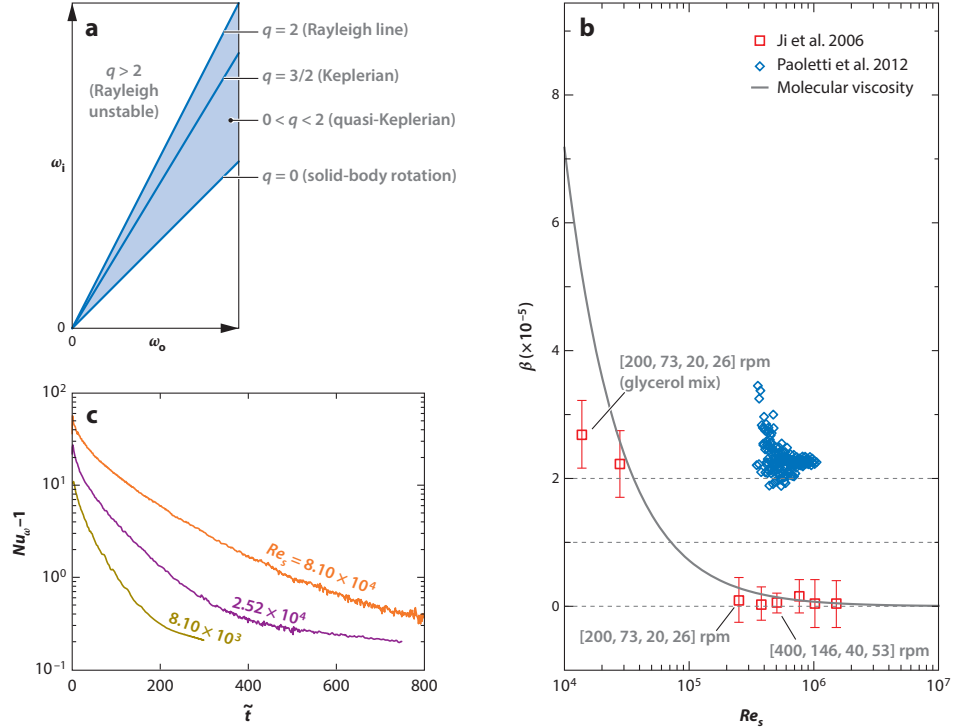


Figure 12

(a) TC parameter space in the co-rotating regime: The different regions are shown between the three lines of constant q , characterising the Rayleigh criterion ($q = 2$), the Keplerian case ($q = 3/2$), and solid-body rotation ($q = 0$). Figure taken from Nordsiek et al. (2015). (b) Dimensionless turbulent viscosity β vs. the shear Reynolds number Re_s . The black line is the molecular viscous value: $\beta_{vic} = \nu / [\bar{r}^3 (\omega_i - \omega_o) / d] = \frac{16\eta(1-\eta)^2}{(1+\eta)^4} Re_s^{-1}$, where $\bar{r} = (r_o + r_i) / 2$. Figure adapted from Ji et al. (2006) and Paoletti et al. (2012). (c) Semi-log time series of $Nu_\omega - 1$ at the inner cylinder for $Ro^{-1} = 1.22$ (implying $q = 1.5$) and three values of the shear Reynolds number, namely $Re_s = 8.10 \times 10^3$ (black line), $Re_s = 2.52 \times 10^4$ (blue dashed line), and $Re_s = 8.10 \times 10^4$ (red dashed-dotted line). Figure taken from Ostilla-Mónico et al. (2014d).

turbulent viscosity β as a function of Re_s is shown in figure 12b. At $Re_s \simeq 7 \times 10^5$ it is $\beta \approx 2 \times 10^{-5}$, which is much larger than the corresponding value of the laminar viscous transport, thus suggesting turbulent behavior. Extrapolating towards astrophysical Reynolds number ($\sim 10^{13}$) by using the formula of F. Hersant, B. Dubrulle & J.-M. Huré (2005), Paoletti et al. (2012) estimated that then $\beta \approx 7.5 \times 10^{-6}$, which is consistent with the values observed in disks around T Tauri stars (7×10^{-8} to 3.5×10^{-5}). However, by means of Laser Doppler Anemometry (LDA) of the azimuthal velocity profiles in the quasi-Keplerian regime in the T³C facility, Nordsiek et al. (2015) found that the angular momentum is transported axially to the axial boundaries, suggesting that TC flow with end plates attached to the outer cylinder is an imperfect model for accretion disk flows.

Ji et al. (2006) studied the angular momentum transport in TC flow in the quasi-

Keplerian regime with a different experimental setup. The radius ratio and aspect ratio were $\eta = 0.35$ and $\Gamma = 2.1$, respectively. In order to minimize Ekman circulation, the end plates were split into two rings that could independently rotate (with the rotation rates of ω_3 and ω_4) with respect to the inner and outer cylinders. By carefully controlling the rotation speeds [$\omega_i, \omega_3, \omega_4, \omega_o$], the azimuthal velocity profiles in the gap were tuned to match the quasi-Keplerian flow profiles, $\Omega(r) = r^q$ with $0 < q < 2$. The angular momentum transport was quantified by measuring the local angular velocity flux, $\rho r \langle u'_\theta u'_r \rangle_t$, where u'_θ and u'_r were the instantaneous velocity fluctuations in radial and azimuthal directions, and $\langle \rangle_t$ stands for averaging over time. The experimental results for β versus Re_s are shown as open squares in figure 12b. When the end-ring plates were optimized to produce Couette profiles, the values of β were found to be around 0.72×10^{-6} with a standard deviation of 2.7×10^{-6} at Re_s from 3×10^5 to 2×10^6 . These values are indistinguishable from the corresponding molecular viscous transport as shown with the solid line in the figure. The work by Ji et al. (2006) thus demonstrates that the axial boundaries can profoundly influence linearly stable flows and purely hydrodynamic quasi-Keplerian flows, under proper boundary conditions and at large enough Reynolds numbers, but cannot transport angular momentum at astrophysically relevant rates.

To settle the issue of end plate effects, Avila (2012) performed direct numerical simulations using both Maryland (Paoletti & Lathrop 2011) and Princeton (Ji et al. 2006) TC geometries at Re_s up to 6.5×10^3 . He found that the end ring plates do drive secondary flows that enhance the global angular momentum transport in both the Maryland and the Princeton geometry. His studies thus indicate that the current laboratory TC apparatuses designed to approximate flow profiles of accretion disks suffer from the imposed boundary conditions (end plates and finite aspect ratio). However, one would also expect that with increasing Re_s the effect of the end plates will get less, as suggested by figure 12b.

To completely prevent end plate effects on the transition, Ostilla-Mónico et al. (2014d) investigated this issue numerically, using periodic boundary conditions in the axial direction at high Reynolds numbers. The shear Reynolds number they achieved in their direct numerical simulations (DNS) was up to 10^5 with a radius ratio of 0.5. The procedures they used for the simulations were as follows: The simulations started with a turbulent field, corresponding to a pure inner cylinder rotation in the laboratory frame ($a = 0, Ro^{-1} = 0$). Then the outer cylinder was switched on such that the rotation ratio was in the quasi-Keplerian regime. As shown in figure 12c, the Nusselt number decreased as a function of time down to a value corresponding to purely non-vortical laminar flow. This work thus showed not only that the TC system at $0 < q < 2$ is linearly stable in this geometry, but that even an initially turbulent flow with shear large Reynolds numbers up to 10^5 decays towards the linearly stable regime, due to stabilizing counter-rotation. This finding is consistent with the experimental results by Edlund & Ji (2014). Figure 12c also shows that the decay time for turbulence becomes longer with increasing shear Reynolds number.

In summary, the present evidence (Ji et al. 2006; Ostilla-Mónico et al. 2014d; Edlund & Ji 2014) indicates that the TC system in the quasi-Keplerian regime is linearly stable at shear Reynolds number up to $Re_s \sim 10^5 - 10^6$. However, one cannot exclude subcritical transitions to turbulence in the quasi-Keplerian regime for TC flow at much higher shear Reynolds numbers and it is thus necessary to examine the TC system at much higher shear Reynolds numbers.

We also note that for $q < 0$, i.e., linearly stable but outside the quasi-Keplerian regime, subcritical transitions to turbulence may occur: E.g. Borrero-Echeverry, Schatz & Tagg

(2010) studied the decay characteristics in TC flow for pure outer cylinder rotation at intermediate Reynolds numbers (up to $Re_o \sim 10^4$) and found a subcritical transition to turbulence. Also Burin & Czarnocki (2012) performed experiments for pure outer cylinder rotation, finding subcritical transitions to spiral or intermittent turbulence, too, which strongly depended on the radius ratio η and the chosen end-cap configurations.

7. Summary and outlook

Summary points:

- The last decade has witnessed a tremendous extension of the experimentally and numerically studied TC parameter space towards the strongly turbulent regime, including co- and counter-rotation of the cylinders.
- In the *classical regime* the bulk is turbulent and the BLs are of Prandtl-Blasius (laminar) type, whereas in the *ultimate regime* also the BLs have become turbulent, i.e., are of Prandtl-von Kármán type. The transition towards the ultimate regime occurs around $Ta^* \simeq 3 \times 10^8$ (for $\eta = 0.71$). Due to the more efficient mechanical driving this is much earlier than in the analogous, but thermally driven RB system, where the transition towards the ultimate regime occurs at $Ra^* \simeq 10^{14}$.
- In the classical regime, for pure inner cylinder rotation the effective scaling exponent γ of $Nu_\omega \sim Ta^\gamma$ is less than $1/3$, whereas in the ultimate regime, for any rotation ratio γ is larger than $1/3$ and follows the theoretical prediction of $Nu_\omega \sim Ta^{1/2} \times$ log-corrections.
- At large enough Taylor number, Nu_ω has a non-monotonic dependence on the (negative) rotation ratio a with a pronounced maximum at $a_{opt} > 0$, at which the angular velocity transport is optimal. The value a_{opt} depends on η : It increases with increasing η for $\eta \lesssim 0.8$ and seems to saturate at larger η .
- For optimal Nu_ω the angular velocity profile is flat and the flow displays pronounced Taylor rolls, in spite of the strong turbulence. The roll structure allows for the existence of multiple turbulent states with different transport and flow properties.
- For large enough Ta, the profiles of the BLs in the ultimate regime are well described by a log-law for the angular velocity, $\Omega^+(\rho^+) = \kappa^{-1} \log \rho^+ + B$, with the well-known von Kármán constant $\kappa \approx 0.4$.
- The current laboratory TC apparatuses designed to approximate flow profiles of accretion disks suffer from the imposed boundary conditions in axial direction. The present experiments and numerical simulations suggest that the TC system in the quasi-Keplerian regime is linearly stable for shear Reynolds number up to $Re_s \sim 10^5 - 10^6$ and presumably beyond, where hitherto no experiments exist. But note that the shear Reynolds numbers relevant in astrophysical circumstellar disks are as large as 10^{13} and higher (F. Hersant, B. Dubrulle & J.-M. Huré 2005).

Future issues:

- A rigorous theoretical understanding of the dependence of a_{opt} on η is still missing. In particular, for $\eta \rightarrow 1$ different mechanisms may be at play as compared to the situation at smaller η on which we focused here.
- In the other limiting case at very small radius ratios $\eta \rightarrow 0$ future investigations are needed, helping to quantitatively examine the curvature effects of the cylinders. One

should also try to understand why the transitional Taylor number Ta^* to the ultimate regime becomes larger at smaller radius ratios.

- When further increasing Ta to $Ta \gg 10^{13}$: Will the large-scale coherent structures (turbulent Taylor rolls) continue to exist? If so, will multiple turbulent states still coexist or will the fluctuation be so large that the turbulent dynamics meanders between these states?
- The review did not touch upon the statistics of the turbulent fluctuations, structure functions, and spectra. Lathrop, Fineberg & Swinney (1992a) and Huisman, Lohse & Sun (2013) experimentally showed that these are different as compared to homogeneous isotropic turbulence, but the reason is unknown.
- As the TC system is closed and can be very well controlled, it is excellently suited to study *multiphase* turbulent flows, i.e., flows with particles, droplets, bubbles (van den Berg et al. 2005, 2007; van Gils et al. 2013), and even with vapor bubbles nucleating close to phase transitions.
- For the same reasons the TC system is very well suited to study the interaction of turbulence with rough walls (Cadot et al. 1997; van den Berg et al. 2003), with superhydrophobic wall (Srinivasan et al. 2015), and with micro- and nano-structured walls, where the structures are either of geometric or of chemical nature.

Disclosure statement

The authors are not aware of any biases that might be perceived as affecting the objectivity of this review.

Acknowledgements

We thank all our coworkers and colleagues for their contributions to our understanding of this great problem, for the many stimulating discussions we had the privilege to enjoy with them over the years, and for their valuable comments on this manuscript. – We also gratefully acknowledge FOM, STW, NWO, and ERC (via an Advanced Grant) for financial support over the years.

LITERATURE CITED

- Ahlers G. 1974. Low temperature studies of the Rayleigh-Bénard instability and turbulence. *Phys. Rev. Lett.* 33:1185–1188
- Ahlers G, Bodenschatz E, He X. 2014. Logarithmic temperature profiles of turbulent rayleighbnard convection in the classical and ultimate state for a prandtl number of 0.8. *J. Fluid Mech.* 758:436–467
- Ahlers G, Grossmann S, Lohse D. 2009. Heat transfer and large scale dynamics in turbulent Rayleigh-Bénard convection. *Rev. Mod. Phys.* 81:503–537
- Andreck CD, Liu SS, Swinney HL. 1986. Flow regimes in a circular Couette system with independently rotating cylinders. *J. Fluid Mech.* 164:155–183
- Avila M. 2012. Stability and angular-momentum transport of fluid flows between co-rotating cylinders. *Phys. Rev. Lett.* 108:124501
- Behringer RP. 1985. Rayleigh-Bénard convection and turbulence in liquid-helium. *Rev. Mod. Phys.* 57:657–687

- Bilson M, Bremhorst K. 2007. Direct numerical simulation of turbulent Taylor-Couette flow. *J. Fluid Mech.* 579:227–270
- Bodenschatz E, Pesch W, Ahlers G. 2000. Recent developments in Rayleigh-Bénard convection. *Ann. Rev. Fluid Mech.* 32:709–778
- Borrero-Echeverry D. 2014. Subcritical transition to turbulence in Taylor-Couette flow. Ph.D. Thesis, Georgia Institute of Technology, USA
- Borrero-Echeverry D, Schatz MF, Tagg R. 2010. Transient turbulence in Taylor-Couette flow. *Phys. Rev. E* 81:025301
- Brauckmann HJ, Eckhardt B. 2013a. Direct numerical simulations of local and global torque in Taylor-Couette flow up to $Re = 30\,000$. *J. Fluid Mech.* 718:398–427
- Brauckmann HJ, Eckhardt B. 2013b. Intermittent boundary layers and torque maxima in Taylor-Couette flow. *Phys. Rev. E* 87:033004
- Büchel P, Lücke M, Roth D, Schmitz R. 1996. Pattern selection in the absolutely unstable regime as a nonlinear eigenvalue problem: Taylor vortices in axial flow. *Phys. Rev. E* 53:4764–4777
- Burin MJ, Czarnocki CJ. 2012. Subcritical transition and spiral turbulence in circular Couette flow. *J. Fluid Mech.* 709:106–122
- Busse FH. 1967. The stability of finite amplitude cellular convection and its relation to an extremum principle. *J. Fluid Mech.* 30:625–649
- Cadot O, Couder Y, Daerr A, Douady S, Tsinober A. 1997. Energy injection in closed turbulent flows: Stirring through boundary layers versus inertial stirring. *Phys. Rev. E* 56:427–433
- Chandrasekhar S. 1981. Hydrodynamic and hydromagnetic stability. New York: Dover
- Chossat P, Iooss G. 1994. The Couette-Taylor problem. New York: Springer
- Chouippe A, Climent E, Legendre D, Gabillet C. 2014. Numerical simulation of bubble dispersion in turbulent Taylor-Couette flow. *Phys. Fluids* 26:043304
- Coles D. 1965. Transition in circular Couette flow. *J. Fluid Mech.* 21:385–425
- Coughlin K, Marcus PS. 1996. Turbulent Bursts in Couette-Taylor Flow. *Phys. Rev. Lett.* 77:2214–2217
- Cross MC, Hohenberg PC. 1993. Pattern formation outside of equilibrium. *Rev. Mod. Phys.* 65:851–1112
- DiPrima RC, Swinney HL. 1981. Instabilities and transition in flow between concentric rotating cylinders. *Hydrodynamic Instabilities and the Transition to Turbulence* (ed. H. L. Swinney & J. P. Gollub), Springer. :139–180
- Doering C, Constantin P. 1994. Variational bounds on energy-dissipation in incompressible flow: shear flow. *Phys. Rev. E* 49:4087–4099
- Dong S. 2007. Direct numerical simulation of turbulent Taylor-Couette flow. *J. Fluid Mech.* 587:373–393
- Dong S. 2008. Turbulent flow between counter-rotating concentric cylinders: a direct numerical simulation study. *J. Fluid Mech.* 615:371–399
- Donnelly RJ. 1991. Taylor-Couette flow: the early days. *Phys. Today* 44(11):32–39
- Drazin P, Reid WH. 1981. Hydrodynamic stability. Cambridge: Cambridge University Press
- Dubrulle B, Dauchot O, Daviaud F, Longgaretti PY, Richard D, Zahn JP. 2005. Stability and turbulent transport in Taylor-Couette flow from analysis of experimental data. *Phys. Fluids* 17:095103
- Dubrulle B, Hersant F. 2002. Momentum transport and torque scaling in Taylor-Couette flow from an analogy with turbulent convection. *Eur. Phys. J. B* 26:379–386
- Eckhardt B, Grossmann S, Lohse D. 2000. Scaling of global momentum transport in Taylor-Couette and pipe flow. *Eur. Phys. J. B* 18:541–544
- Eckhardt B, Grossmann S, Lohse D. 2007a. Fluxes and energy dissipation in thermal convection and shear flows. *Europhys. Lett.* 78:24001
- Eckhardt B, Grossmann S, Lohse D. 2007b. Torque scaling in turbulent Taylor-Couette flow between independently rotating cylinders. *J. Fluid Mech.* 581:221–250

- Eckhardt B, Schneider T, Hof B, Westerweel J. 2007. Turbulence transition in pipe flow. *Annu. Rev. Fluid Mech.* 39:447–468
- Edlund EM, Ji H. 2014. Nonlinear stability of laboratory quasi-Keplerian flows. *Phys. Rev. E* 89:021004(R)
- Esser A, Grossmann S. 1996. Analytic expression for Taylor-Couette stability boundary. *Phys. Fluids* 8:1814–1819
- F. Hersant, B. Dubrulle, J.-M. Huré. 2005. Turbulence in circumstellar disks. *Astron. & Astrophys.* 429:531–542
- Fardin MA, Perge C, Taberlet N. 2014. “The hydrogen atom of fluid dynamics” - Introduction to the Taylor-Couette flow for Soft Matter scientists. *Soft Matter* 10:3523–3535
- Fenstermacher PR, Swinney HL, Gollub JP. 1979. Dynamical instabilities and the transition to chaotic Taylor vortex flow. *J. Fluid Mech.* 94:103–128
- Gebhardt T, Grossmann S. 1993. The Taylor-Couette eigenvalue problem with independently rotating cylinders. *Z. Physik B* 90:475–490
- Grossmann S. 2000. The onset of shear flow turbulence. *Rev. Mod. Phys.* 72:603–618
- Grossmann S, Lohse D. 2000. Scaling in thermal convection: A unifying view. *J. Fluid. Mech.* 407:27–56
- Grossmann S, Lohse D. 2001. Thermal convection for large Prandtl number. *Phys. Rev. Lett.* 86:3316–3319
- Grossmann S, Lohse D. 2002. Prandtl and Rayleigh number dependence of the Reynolds number in turbulent thermal convection. *Phys. Rev. E* 66:016305
- Grossmann S, Lohse D. 2004. Fluctuations in turbulent Rayleigh-Bénard convection: The role of plumes. *Phys. Fluids* 16:4462–4472
- Grossmann S, Lohse D. 2011. Multiple scaling in the ultimate regime of thermal convection. *Phys. Fluids* 23:045108
- Grossmann S, Lohse D. 2012. Logarithmic temperature profiles in the ultimate regime of thermal convection. *Phys. Fluids* 24:125103
- Grossmann S, Lohse D, Sun C. 2014. Velocity profiles in strongly turbulent Taylor-Couette flow. *Phys. Fluids* 26:025114
- He W, Tanahashi M, Miyauchi T. 2007. Direct numerical simulation of turbulent Taylor-Couette flow with high Reynolds number. *Advances in Turbulence XI: Proceedings of the 11th EUROMECH European Turbulence Conference held June 25-28, 2007, in Porto, Portugal*
- He X, Funfschilling D, Bodenschatz E, Ahlers G. 2012a. Heat transport by turbulent Rayleigh-Bénard convection for $Pr = 0.8$ and $4 \times 10^{11} \lesssim Ra \lesssim 2 \times 10^{14}$: ultimate-state transition for aspect ratio $\Gamma = 1.00$. *New J. Phys.* 14:063030
- He X, Funfschilling D, Nobach H, Bodenschatz E, Ahlers G. 2012b. Transition to the ultimate state of turbulent Rayleigh-Bénard convection. *Phys. Rev. Lett.* 108:024502
- Howard LN. 1972. Bounds on flow quantities. *Ann. Rev. Fluid. Mech.* 4:473–494
- Hristova H, Roch S, Schmid P, Tuckerman L. 2002. Transient growth in Taylor-Couette flow. *Phys. Fluids* 14:3475–3484
- Huisman SG, Lohse D, Sun C. 2013. Statistics of turbulent fluctuations in counter-rotating Taylor-Couette flows. *Phys. Rev. E* 88:063001
- Huisman SG, Scharnowski S, Cierpka C, Kähler C, Lohse D, Sun C. 2013. Logarithmic boundary layers in strong Taylor-Couette turbulence. *Phys. Rev. Lett.* 110:264501
- Huisman SG, van der Veen RCA, Sun C, Lohse D. 2014. Multiple states in highly turbulent Taylor-Couette flow. *Nat. Commun.* 5:3820
- Huisman SG, van Gils DPM, Grossmann S, Sun C, Lohse D. 2012. Ultimate turbulent Taylor-Couette flow. *Phys. Rev. Lett.* 108:024501
- Hultmark M, Vallikivi M, Bailey SCC, Smits AJ. 2012. Turbulent pipe flow at extreme Reynolds numbers. *Phys. Rev. Lett.* 108:094501
- Ji H, Balbus S. 2013. Angular momentum transport in astrophysics and in the lab. *Phys. Today*

- Ji H, Burin M, Schartman E, Goodman J. 2006. Hydrodynamic turbulence cannot transport angular momentum effectively in astrophysical disks. *Nature* 444:343–346
- Kadanoff LP. 2001. Turbulent heat flow: Structures and scaling. *Phys. Today* 54:34–39
- Koschmieder EL. 1993. Bénard cells and Taylor vortices. Cambridge: Cambridge University Press
- Kraichnan RH. 1962. Turbulent thermal convection at arbitrary Prandtl number. *Phys. Fluids* 5:1374–1389
- Landau LD, Lifshitz EM. 1987. Fluid mechanics. Oxford: Pergamon Press
- Lathrop DP, Fineberg J, Swinney HS. 1992a. Transition to shear-driven turbulence in Couette-Taylor flow. *Phys. Rev. A* 46:6390–6405
- Lathrop DP, Fineberg J, Swinney HS. 1992b. Turbulent flow between concentric rotating cylinders at large Reynolds numbers. *Phys. Rev. Lett.* 68:1515–1518
- Lewis GS, Swinney HL. 1999. Velocity structure functions, scaling, and transitions in high-Reynolds-number Couette-Taylor flow. *Phys. Rev. E* 59:5457–5467
- Lohse D, Xia KQ. 2010. Small-scale properties of turbulent Rayleigh-Bénard convection. *Ann. Rev. Fluid Mech.* 42:335–364
- Lord Rayleigh. 1917. On the dynamics of revolving fluids. *Proceedings of the Royal Society of London Series A* 93 (648)
- Lorenz EN. 1963. Deterministic nonperiodic flow. *J. Atmos. Sci* 20:130–141
- Maretzke S, Hof B, Avila M. 2014. Transient growth in linearly stable Taylor-Couette flows. *J. Fluid Mech.* 742:254–290
- Marques F, Lopez J. 1997. Taylor-Couette flow with axial oscillations of the inner cylinder: Floquet analysis of the basic flow. *J. Fluid Mech.* 348:153–175
- Marusic I, McKeon BJ, Monkewitz PA, Nagib HM, Smits AJ, Sreenivasan KR. 2010. Wall-bounded turbulent flows at high Reynolds numbers: Recent advances and key issues. *Phys. Fluids* 22:065103
- Merbold S, Brauckmann HJ, Egbers C. 2013. Torque measurements and numerical determination in differentially rotating wide gap Taylor-Couette flow. *Phys. Rev. E* 87:023014
- Meseguer A. 2002. Energy transient growth in the Taylor-Couette problem. *Phys. Fluids* 14:1655–1660
- Mullin T, Cliffe KA, Pfister G. 1987. Unusual time-dependent phenomena in Taylor-Couette flow at moderately low Reynolds numbers. *Phys. Rev. Lett.* 58:2212–2215
- Nordsiek F, Huisman SG, van der Veen RCA, Sun C, Lohse D, Lathrop DP. 2015. Azimuthal velocity profiles in rayleigh-stable Taylor-Couette flow and implied axial angular momentum transport. *ArXiv* :1408.1059v2
- Ostilla-Mónico R, Huisman SG, Jannink TJG, Van Gils DPM, Verzicco R, et al. 2014a. Optimal Taylor-Couette flow: radius ratio dependence. *J. Fluid Mech.* 747:1–29
- Ostilla-Mónico R, Stevens RJAM, Grossmann S, Verzicco R, Lohse D. 2013. Optimal Taylor-Couette flow: direct numerical simulations. *J. Fluid Mech.* 719:14–46
- Ostilla-Mónico R, van der Poel EP, Verzicco R, Grossmann S, Lohse D. 2014b. Boundary layer dynamics at the transition between the classical and the ultimate regime of Taylor-Couette flow. *Phys. Fluids* 26:015114
- Ostilla-Mónico R, van der Poel EP, Verzicco R, Grossmann S, Lohse D. 2014c. Exploring the phase diagram of fully turbulent Taylor-Couette flow. *J. Fluid Mech.* 761:1–26
- Ostilla-Mónico R, Verzicco R, Grossmann S, Lohse D. 2014d. Turbulence decay towards the linearly stable regime of Taylor-Couette flow. *J. Fluid Mech.* 748:R3
- Paoletti MS, Lathrop DP. 2011. Angular momentum transport in turbulent flow between independently rotating cylinders. *Phys. Rev. Lett.* 106:024501
- Paoletti MS, van Gils DPM, Dubrulle B, Sun C, Lohse D, Lathrop DP. 2012. Angular momentum transport and turbulence in laboratory models of Keplerian flows. *Astron. & Astrophys.* 547:A64
- Pfister G, Rehberg I. 1981. Space dependent order parameter in circular Couette flow transitions.

Phys. Lett. 83:19–22

- Pirro D, Quadrio M. 2008. Direct numerical simulation of turbulent Taylor-Couette flow. *Eur. J. Mech. B-Fluids* 27:552–566
- Ravelet F, Delfos R, Westerweel J. 2010. Influence of global rotation and Reynolds number on the large-scale features of a turbulent Taylor–Couette flow. *Phys. Fluids* 22:055103
- Richard D. 2001. Instabilités hydrodynamiques dans les écoulements en rotation différentielle. Ph.d. thesis, Université Paris-Diderot - Paris VII
- Richard D, Zahn J. 1999. Turbulence in differentially rotating flows – What can be learned from the Couette-Taylor experiment. *Astron. & Astrophys.* 347:734–738
- Roche PE, Gauthier G, Kaiser R, Salort J. 2010. On the triggering of the ultimate regime of convection. *New J. Phys.* 12:085014
- Schartman E, Ji H, Burin MJ. 2009. Development of a Couette-Taylor flow device with active minimization of secondary circulation. *Rev. Sci. Instr.* 80(2):024501
- Schartman E, Ji H, Burin MJ, Goodman J. 2012. Stability of quasi-keplerian shear flow in a laboratory experiment. *Astron. & Astrophys.* 543:A94
- Siggia ED. 1994. High Rayleigh number convection. *Annu. Rev. Fluid Mech.* 26:137–168
- Smith GP, Townsend AA. 1982. Turbulent Couette flow between concentric cylinders at large Taylor numbers. *J. Fluid Mech.* 123:187–217
- Smits AJ, Marusic I. 2013. Wall-bounded turbulence. *Phys. Today* 66:25–30
- Smits AJ, McKeon BJ, Marusic I. 2010. High-Reynolds number wall turbulence. *Annu. Rev. Fluid Mech.* 43:353–375
- Srinivasan S, Kleingartner JA, Gilbert JB, Cohen RE, Milne AJB, McKinley GH. 2015. Sustainable drag reduction in turbulent Taylor-Couette flows by depositing sprayable superhydrophobic surfaces. *Phys. Rev. Lett.* 114:014501
- Strogatz SH. 1994. Nonlinear dynamics and chaos. Reading: Perseus Press
- Tagg R. 1994. The Couette-Taylor problem. *Nonlinear Science Today* 4(3):1–25
- Taylor GI. 1923. Stability of a viscous liquid contained between two rotating cylinders. *Phil. Trans. R. Soc. A* 223:289–343
- Taylor GI. 1936. Fluid friction between rotating cylinders. *Proc. R. Soc. London A* 157:546–564
- Tong P, Goldburg WI, Huang JS, Witten TA. 1990. Anisotropy in turbulent drag reduction. *Phys. Rev. Lett.* 65:2780–2783
- Trefethen L, Trefethen A, Reddy S, Driscoll T. 1993. Hydrodynamic stability without eigenvalues. *Science* 261:578–584
- Tuckerman LS. 2014. Taylor vortices versus Taylor columns. *J. Fluid Mech.* 750:1–4
- van den Berg TH, Doering C, Lohse D, Lathrop D. 2003. Smooth and rough boundaries in turbulent Taylor-Couette flow. *Phys. Rev. E* 68:036307
- van den Berg TH, Luther S, Lathrop DP, Lohse D. 2005. Drag reduction in bubbly Taylor-Couette turbulence. *Phys. Rev. Lett.* 94:044501
- van den Berg TH, van Gils DPM, Lathrop DP, Lohse D. 2007. Bubbly turbulent drag reduction is a boundary layer effect. *Phys. Rev. Lett.* 98:084501
- van Gils DPM, Bruggert GW, Lathrop DP, Sun C, Lohse D. 2011a. The Twente turbulent Taylor-Couette (T^3C) facility: strongly turbulent (multi-phase) flow between independently rotating cylinders. *Rev. Sci. Instr.* 82:025105
- van Gils DPM, Huisman SG, Bruggert GW, Sun C, Lohse D. 2011b. Torque scaling in turbulent Taylor-Couette flow with co- and counter-rotating cylinders. *Phys. Rev. Lett.* 106:024502
- van Gils DPM, Huisman SG, Grossmann S, Sun C, Lohse D. 2012. Optimal Taylor-Couette turbulence. *J. Fluid Mech.* 706:118–149
- van Gils DPM, Narezo-Guzman D, Sun C, Lohse D. 2013. The importance of bubble deformability for strong drag reduction in bubbly turbulent Taylor-Couette flow. *J. Fluid Mech.* 722:317–347
- van Hout R, Katz J. 2011. Measurements of mean flow and turbulence characteristics in high-Reynolds number counter-rotating Taylor-Couette flow. *Phys. Fluids* 23:105102

- Wendt F. 1933. Turbulente Strömungen zwischen zwei rotierenden Zylindern. *Ingenieurs-Archiv* 4:577–595
- Zagarola MV, Smits AJ. 1998. Mean-flow scaling of turbulent pipe flow. *J. Fluid Mech.* 373:33–79